



Skolkovo Institute of Science and Technology

DATA-DRIVEN DESIGN OF MULTICOMPONENT
ALLOYS

Doctoral Thesis

by

VADIM SOTSKOV

DOCTORAL PROGRAM IN MATERIALS SCIENCE AND
ENGINEERING

Supervisor
Full Professor, Alexander Shapeev

Moscow – 2023

© Vadim Sotskov, 2023

I hereby declare that the work presented in this thesis was carried out by myself at Skolkovo Institute of Science and Technology, Moscow, except where due acknowledgement is made, and has not been submitted for any other degree.

Candidate (Vadim Sotskov)

Supervisor (Prof. Alexander Shapeev)

Data-driven Design of Multicomponent Alloys

by

Vadim Sotskov

Tuesday 28th November, 2023 00:06

Submitted to the Skoltech Center of Research, Entrepreneurship and Innovation on November 2023, in partial fulfillment of the requirements for the Doctoral Program in Materials Science and Engineering

Abstract

In this work I propose a methodology for designing multicomponent alloys using on-lattice modeling. This approach assumes that the simulated system has an ideal lattice with fixed atomic positions. Thus, an energy minimum of a structure is found by adjusting a chemical ordering on an ideal lattice. Such type of simulations is computationally cheap and can be effectively used for modeling multicomponent materials.

In my work I show how on-lattice simulations can be used in two tasks of multicomponent materials modeling, namely, crystal structure prediction (CSP) at zero temperature and modeling phase stability when the temperature is finite. For that I developed two separate approaches, both based on an on-lattice structure generation algorithm and on-lattice machine learning interatomic potentials. For the prediction of ground state structures I developed a novel structure generation algorithm, that can automatically generate configurations with different chemical composition. By combining this algorithm with cluster expansion (CE) and the low-rank potential (LRP) I constructed convex hull of binary, ternary and quaternary systems. The developed methodology was named “on-lattice CSP”. For modeling phase stability at finite temperatures I used the well established combination of on-lattice canonical Monte Carlo (CMC) method with the low-rank potential and extended it to investigation of a phase stability in high-entropy carbides. In each simulation method LRP and CE are fitted to energies of the structures relaxed with DFT.

In this work, on-lattice CSP was used to predict stable binary, ternary and quaternary compounds in Nb-Mo-Ta-W chemical space. The results were compared to those reported in AFLOW database, and a dozen of new ground states were found.

Next, using the on-lattice CMC I investigated phase stability of TiZrNbHfTaC₅ high-entropy carbide. The simulations revealed the phase transition from several chemically random phases to a solid solution at 1200 K as was also confirmed by experiments.

Finally, the on-lattice CMC and LRP were applied to study short-range order in CrCoNi alloy. The presence of short range order was observed at temperatures up to 900 K. The impact of magnetism was observed to be negligible on the ordering behaviour.

These computational experiments demonstrate the efficiency of the proposed methodology in studying the mentioned systems and, moreover, show that it can be used for a rational design of other multicomponent materials.

Publications

Main author

1. Vadim Sotskov, Evgeny V. Podryabinkin, and Alexander V. Shapeev. A machine-learning potential-based generative algorithm for on-lattice crystal structure prediction. *Journal of Materials Research*, 2023
2. Alexander Ya. Pak, Vadim Sotskov, Arina A. Gumovskaya, Yuliya Z. Vassilyeva, Zhanar S. Bolatova, Yulia A. Kvashnina, Gennady Ya. Mamontov, Alexander V. Shapeev, and Alexander G. Kvashnin. Machine learning-driven synthesis of TiZrNbHfTaC_5 high-entropy carbide. *npj Computational Materials*, 9(1):7, 2023

Co-author

1. Sheuly Ghosh, Vadim Sotskov, Alexander V. Shapeev, Jörg Neugebauer, and Fritz Körmann. Short-range order and phase stability of crconi explored with machine learning potentials. *Phys. Rev. Mater.*, 6:113804, 2022

Dedicated to my parents.

Acknowledgments

I want to thank my supervisor Prof. Alexander Shapeev, who inspired me to explore new horizons in computational material science, machine learning, and scientific computing. I also want to thank Evgeny Podryabinkin, who helped a lot with the technical stuff at the beginning of my PhD studies.

I want to give thanks to collaborators in my research work, namely Alexander Kvashnin, Fritz Körmann and Sheuly Ghosh. I also want to thank all group mates: Ivan Novikov, Tatiana Kostiuchenko, Eugenio Tsymbalov, and Max Hodapp. They were always ready to help me with technical issues and discussing possible solutions.

Finally, I want to thank Skoltech for the provided unique and fruitful scientific environment, and a possibility to grow as a person.

Contents

1	Introduction	14
2	Background	19
2.1	Limitations of conventional alloying	19
2.2	High-entropy alloys	21
2.3	Computational materials modeling	24
2.3.1	Density functional theory	27
2.3.2	Empirical potentials	29
2.3.3	Machine-learning interatomic potentials	30
2.3.4	Cluster expansion	33
2.3.5	On-lattice low-rank potential	34
2.4	Structure generation methods	36
3	Methodology of multicomponent alloys modeling	39
3.1	On-lattice CSP	39
3.2	On-lattice Canonical Monte Carlo method	43
3.3	Modeling procedure	46
3.3.1	Modeling with on-lattice CSP	46
3.3.2	Modeling with on-lattice Monte Carlo	47
4	Investigation of Nb-Mo-Ta-W system with on-lattice CSP	50
4.1	Calculation details	51
4.2	Nb-W	51
4.3	Mo-Ta-W	53
4.4	Nb-Mo-Ta-W	55
5	Investigation of phase stability of HfTaTiNbZrC₅ high-entropy carbide	59
5.1	Calculation details	60
5.2	Results of HfTaTiNbZrC ₅ study	61
6	Investigation of phase stability and short-range order of CrCoNi	71
6.1	Calculation details	72
6.2	Results of CrCoNi study	73
7	Conclusion	81

8 Appendix	84
8.1 Technical realization of “on-lattice” package	84
Bibliography	88

List of Figures

2-1	Schematic illustration of phases, which may form in HEA. Left - an ideal solid solution; right - ordered intermetallic phase.	22
2-2	Dependence between VEC and phase stability in several HEAs. Blue symbols represent compounds with pure bcc phases; orange - a mixture of bcc and fcc phases; red - compounds with pure fcc phases. . .	24
2-3	Efficiency of atomic interaction approximation methods with corresponding scales of the simulated system.	25
2-4	Illustration of an idea of fitting to <i>ab initio</i> data. Red markers correspond to calculated data (structure/energy), black line illustrates the fitting model.	32
3-1	Illustration the structure “growth” process in on-lattice CSP.	41
3-2	Construction of a first unit cell vector. Centers of identical neighborhoods are connected (a). The growth area is reshaped (b). Outer atoms are translated into a new growth area, conflicting atoms are detected (c). Resolving conflicts by choosing lowest energy configuration (d-e)	42
3-3	Construction of second and third unit cell vectors and final structure.	43
3-4	Schematic illustration of evaluation of energy contribution of an “alchemical” neighborhood.	43
3-5	Illustration of a site exchange during canonical Monte Carlo simulation.	45
3-6	On-lattice CSP modeling procedure.	48
3-7	Convex hull construction with on-lattice CSP simulation. A potentially new point on convex hull is marked with a dashed circle.	49
3-8	Algorithm for obtaining an accurate LRP during on-lattice CMC simulations.	49
4-1	Final DFT Nb-W convex hull and unit cells of the new structures. Six new structures were discovered with on-lattice CSP (marked with red circles on the convex hull).	52
4-2	Final DFT Mo-Ta-W convex hull and unit cells of the new structures. Six new structures were discovered with on-lattice CSP (marked with red on the convex hull).	54

4-3	Final DFT Nb-Mo-Ta-W convex hull and unit cells of the new structures. Two new quaternary structures (9-atom NbMoTaW ₆ and 22-atom NbMo ₂ TaW ₁₈) were discovered. Stable structures discovered with on-lattice CSP are marked with orange circles and squares on the convex hull.	56
5-1	Specific heat capacity $C_V(T)$ for <i>fcc</i> TiZrNbHfTaC ₅ from CMC simulations for a 10 × 12 × 15 simulation box. Vertical dashed line marks the probable phase transition. Blue shaded area indicates a standard deviation calculated from 40 independent runs for each temperature. .	62
5-2	Crystal structures of the simulated 16 × 16 × 16 supercell of a) multi- and b) single-phase (Ti-Zr-Nb-Hf-Ta)C at 500 and 2000 K respectively. Carbon atoms are not shown here explicitly to make the distribution of metal atoms clearer, while carbon atoms were considered in the MC simulations; c,d) relative concentration of chemical elements per layer along the supercell vector <i>b</i>	63
5-3	SEM images of experimental samples with energy dispersive X-ray analysis. a) Single- and b) multi-phase samples. Dispersive X-ray analysis images show the mapping of chemical elements across the sample. 20 points across the sample were used to measure the elemental distributions (shown in the inset).	66
5-4	X-ray diffraction patterns of the synthesized a) single- and b) multi-phase samples of TiZrNbHfTaC ₅ , and calculated XRD patterns of c) simulated single-phase HEC, and d) separate phases of ZrHfTaC ₃ , ZrNbHfC ₃ , ZrNbHfTaC ₄ , ZrNbC ₂ , ZrTaC ₂ , and TiNbTaC ₃ found by the analysis of calculated Helmholtz free energies of mixing of various multi-component carbides.	67
5-5	Simulated HEC containing 64000 atoms (32000 of metal atoms and 32000 carbons) at 500 K. Carbon atoms are not explicitly displayed here to make the distribution of metal atoms clearer. Immiscibility of TiC with HfC and ZrC is clearly seen, while NbC and TaC are perfectly mixed with all other carbides. Cavities where no carbides were observed except selected ones are shown by black color.	68
5-6	Correlation between the Helmholtz free energy of mixing as calculated at 500 K and the lattice parameters of binary (circles), ternary (squares), quaternary (triangles) carbides and HEC (star). Horizontal dashed lines and shaded areas represent lattice parameters and error of the experimentally observed phases respectively.	69
6-1	Specific heat capacity $C_V(T)$ for <i>fcc</i> CrCoNi from CMC simulations for a 6 × 6 × 6 and 12 × 12 × 12 simulation box.	73
6-2	Simulated structures. (a) CrCo ₂ +CrNi ₂ obtained at 50 K. (b) Cr(Co,Ni) ₂ obtained at 510 K. (c) Random solid solution obtained at very high temperature.	74

6-3	Temperature-dependent Warren-Cowley SRO parameters for different atom pairs in the first coordination shell in CrCoNi alloy. The panels demonstrate qualitatively different nature of the low- and high-temperature transitions.	75
6-4	DFT calculated energy differences as compared to a random alloy for the two ordered states found in the present work as well as previous works. The calculations include purely ionic relaxations (red) as well as full relaxation (green). The impact of electronic excitations (light red and light green) are shown as well. The DFT calculated energy differences found in previous works (blue shades) by Pei et al. [2020], Tamm et al. [2015] and Walsh et al. [2021] between the random alloy and there proposed ordered state have been also added.	76
6-5	The arrangement of constituent atoms in (a) the presently obtained ordered structure (in case of cubic supercell) of CrCoNi at a temperature of 510 K compared with (c) the ground state structure as suggested by Pei et al. [2020]. In case of (a), for clear visualization of our obtained Cr(Co,Ni) ₂ structure, only a certain part of the 864-atom cell with smaller boundary is shown. Another orthorhombic primitive cell as considered in case of orthorhombic supercell for Cr(Co,Ni) ₂ structure has been also added in (b) for better visualization. The half-coloured spheres with yellow and red represents the 50% occupancy probability of Co and Ni for those sites.	78
6-6	The calculated temperature dependence of mean internal energies obtained from magnetic and non-magnetic LRP based MC simulations for equiatomic CrCoNi alloy with supercell size 12 × 12 × 12. The energy of high temperature magnetic random solid solution has been included as reference (grey line).	79
8-1	Structure of the developed code.	86

List of Tables

4.1	Position below convex hull of predicted Nb-W alloys.	53
4.2	Formation enthalpies of MoTa-based alloys.	55
5.1	Vacancy formation energies of five metals in the corresponding individual carbides.	70
6.1	Presently calculated low rank potentials (LRP) based Monte Carlo (MC) simulated Warren-Cowley SRO parameters in CrCoNi alloy at a temperature of 500 K compared to previous DFT based Monte Carlo studies by Tamm et al. [2015] and Ding et al. [2018].	77

Chapter 1

Introduction

Availability of new materials is the driving factor in the development of technology. For example, production of surface protection coatings, space vehicle parts or fusion nuclear reactors demands materials with a high phase stability. One class of such materials are metallic alloys. Traditionally, their properties are optimized by adding a small concentration of secondary elements to a principle element such as Al, Fe, Ni, etc. However, such approach substantially limits amount of all possible element combinations and, hence, leaves a huge number of alloys unexplored. One of the alternative approaches to optimize targeted properties of these materials is to mix principal elements in relatively high (often equiatomic) concentration. This led to an emergence of a new class of metallic alloys known as compositionally complex alloys (CCA). Some of the recently discovered examples have outperformed traditional alloys and have shown promising properties such as stability at high temperature, phase stability under irradiation, high hardness, and corrosion resistance [George et al. \[2019\]](#). Therefore, targeted design of such materials is of high priority.

Among these multicomponent materials the most popular subject of theoretical and experimental research are high-entropy alloys (HEA) [Yeh et al. \[2004\]](#) and high-entropy ceramics (HEC) [Castle et al. \[2018\]](#). They usually contain five or more principal chemical components in near equiatomic concentration. One of the factors responsible for stabilization of these materials is a high configurational entropy, which lowers the free energy when multiple components are mixed together. Apart from high entropy, other factors contribute to stabilization of alloy. For example,

local stresses in crystalline lattice, caused by a difference in atomic sizes, slow down diffusion processes, dislocation and grain boundary movements, which leads to stabilization of a solid solution Tsai et al. [2013]. All these factors contribute to excellent mechanical properties, which makes these materials high-valued in different areas of industry.

A traditional way to design materials is to use experimental approach. The most common techniques of synthesising HEA and HEC are melting and casting, and milling followed by consolidation (mostly spark plasma sintering). Both these methods require careful selection of raw materials as well as adjustment and precise control of many parameters such as melting temperature and arc plasma current. Moreover, parameters of a synthesis should be adjusted for each chemical compound separately. Given this, experimental discovery of these materials is a challenging process.

In recent decades, due to rapid development of computational power, a new field of materials science known as computational materials design has emerged. It comprises numerical simulation methods, that allow to investigate behavior of a matter at atomic and electronic scales. These methods can be applied to investigate phase stability Kostiuchenko et al. [2019, 2020], diffusion processes Wu et al. [2016], mechanical properties Kiely et al. [2021] and even predict a crystal structure of a material Lyakhov et al. [2013]. The most accurate are quantum-mechanical (*ab initio*) methods such as density functional theory (DFT) Jensen [2007c].

However, computational efficiency of *ab initio* methods decreases with the increase of the simulation cell. This becomes especially problematic when scales comparable to experiment are required. For that reason, alternative models of interatomic interaction are being actively developed. As a rule, these models interpolate quantum mechanical calculations and, therefore, can produce results of a comparable accuracy. They include, for example, CE Sanchez [2010] and embedded atom model (EAM) Deye et al. [Mar 2013]. However, efficiency of many of these models largely depends on the number of chemical components in the system. Therefore, their application to modeling multicomponent materials can be difficult.

Currently, for simulating multicomponent materials, new class of models are be-

ing developed, namely machine-learning interatomic potentials. One of the first examples was Behler-Parrinello neural networks (BPNN) Behler and Parrinello [2007]. They are still being actively developed and in their last form can account for global charge distribution, which leads to much improved results Ko et al. [2021]. There are many types of other machine-learning potentials like, for example, Gaussian approximation potential (GAP) Bartók et al. [2010] and spectral neighbor analysis potentials (SNAP) Willman et al. [2020]. In principle, all these methods comprise two parts: descriptor and regressor. First one describes the atomic environment and should account for symmetry in interactions - energy should be invariant under rotation, inversion and permutation of identical atoms. The second, regressor, is a functional that maps descriptor onto interaction energies. The potentials listed above use different regressors. Thus, BPNN uses neural networks to predict interaction energies, while GAP is based on gaussian process regression and SNAP - on linear regression.

Among this class of potentials is LRP Shapeev [2017], which has been designed specifically for the study of multicomponent materials. The main feature of this potential is that it learns the energy of atomic environments without accounting for atomic positions, which makes it an “on-lattice” interaction model. This potential has been successfully applied for the study of chemical ordering in a number of multicomponent metallic alloys Kostiuchenko et al. [2019, 2020], Ghosh et al. [2022], Pak et al. [2023].

Another important part of numerical modeling of materials is the generation of a structure along optimization direction. As a rule, standard optimization algorithms are used for this task Nocedal and Wright [2006], Press et al. [1992]. However, these methods work well in local areas of potential energy surface (PES), when geometry of initial configuration is close to the optimal. In most of the cases, energetically favorable areas on PES are not known apriori and other sampling methods are required. One approach is to perform random walks on PES as implemented in Monte Carlo method. A more optimal solution, developed quite recently, is based on the evolutionary methods. The idea consist in applying heredity operators to a set of low energy parent structures in order to create a new population. The

process continues until the most stable structure remains unchanged for a certain number of steps. The most successful implementation of evolutionary algorithms for crystal structure prediction is USPEX code [Lyakhov et al. \[2013\]](#). This method has been successfully applied for discovering thermoelectric materials [Dong et al. \[2019a\]](#), superconductors [Semenok et al. \[2018\]](#) and new stoichiometries of common chemical compounds under a high pressure [Zhang et al. \[2016\]](#).

Even with the aforementioned advances in simulation techniques the problem of multicomponent materials modeling is still acute. The bottleneck consists in probing enormous number of chemical combinations from multicomponent configurational space. As a consequence, only a limited number of discovered multicomponent materials is reported. However, in the case of metallic alloys, an advantage can be derived from their structure. Most of the mechanically stable alloys are described by simple cubic and hexagonal lattices (BCC, FCC, HCP). Thus, the optimal geometry of a material is already known and the task consists in finding the most stable chemical ordering on a fixed lattice. This class of problems is known as "on-lattice" problems and has been applied to investigate phase stability of multicomponent systems [Kostiuchenko et al. \[2019, 2020\]](#), [Ghosh et al. \[2022\]](#), [Pak et al. \[2023\]](#) as well as generating a pool of potentially stable multicomponent metallic alloys [Hart and Forcade \[2008, 2009\]](#), [Hart et al. \[2012\]](#), [Gubaev et al. \[2019\]](#).

The aim of this work is to develop and validate the methodology for modeling multicomponent alloys with on-lattice approach. Specifically, I develop the methods for solving two tasks of materials modeling - crystal structure prediction and modeling phase stability at finite temperatures. The first methodology is based on a structure generation algorithm, called "on-lattice CSP" and it is combined with LRP and CE. The second is a combination of canonical Monte Carlo with LRP.

Author Contribution

In the first work the author has developed the code for on-lattice CSP, performed all the simulations and obtained the results. Also, he prepared the manuscript with the results of the study.

In the second work the author has developed the code for on-lattice CMC, per-

formed all the simulations, obtained the theoretical results and prepared the part of the manuscript where his part of the work is reported. The experimental part of the work was performed and reported by a A. Y. Pak from Tomsk Polytechnic University, Russia.

In the third work the author has developed the code for on-lattice CMC and contributed to the manuscript preparation. The simulations and general preparation of the manuscript were performed by Sheuly Ghosh and Fritz Körmann from Max-Planck-Institut für Eisenforschung GmbH, Düsseldorf, Germany.

The present dissertation was written solely by the author.

Chapter 2

Background

2.1 Limitations of conventional alloying

The problem of designing new materials is crucial for the modern industry. The design process should address the aspects of operational environment, such as mechanical stress, thermal and nuclear irradiation, etc. These conditions, for example, are ubiquitous in production of nuclear fusion reactor shells. When material of a reactor's chamber is subjected to a high-energy irradiation, atoms leave their lattice positions, leading to creation of a Frenkel pair. Accumulation of Frenkel pairs stimulates the formation of complex defects, such as voids, precipitations and dislocations [Zhang et al. \[2018\]](#). As a result, the operational limits of the used materials are dramatically reduced. Different techniques are applied to prolong their durability and improve the structural performance. The most common among them is alloying. This technique consists in adding a small amount of alloying agents in order to improve the primary properties of the main component or invoke the secondary ones. One of the driving factors, causing an alloy strengthening are distortions inside the crystal lattice, induced by alloying additions. Apart from mechanical performance, this technique is used to improve thermal stability, corrosion resistance, conductivity and many other critical properties.

Alloying imply adding secondary elements in concentrations not exceeding 20% of the total materials composition. Such approach is used to manufacture the so-called traditional alloys. Among them, for example, are Al-Li (2.45 % Li), used for

aerospace applications Abd El-Aty et al. [2017], Rioja and Liu [2012], Lavernia et al. [1990], and Be-Co (0.5-3 % Be), used in a wide variety of fields from cryogenic equipment to drilling industry Monzen et al. [2011], Tanner et al. [1988]. Alloying was also applied to synthesize some multicomponent alloys, such as Al-Ni-Co (traditionally 8 % Al, 26 % Ni, 24 % Co and the rest is Fe) Zhou et al. [2017] or cobalt-based Co-Cr-Mo (60 % Co, 20 % Cr, 5 % Mo and other substances) Roudnicka et al. [2021].

However, traditional alloys are represented, as a rule, by compounds synthesised from a single base metal and a small amount of alloying agents. Besides, most of them contain no more than three chemical components. Therefore, conventional alloying strategies are very restrictive in exploring materials containing several main components in nearly equal proportions Cantor [2014]. As a result, a sufficient number of multicomponent alloys remains unexplored. To estimate this number let's consider a system containing m components with concentration tolerance of $c\%$. The total number of possible alloys in this system is defined as follows:

$$N = (100/c)^{m-1} \quad (2.1)$$

Restricting to metallic elements, which are easily accessible in the industry (not rare, toxic, etc.) gives $m = 30$. Taking concentration tolerance of 1% gives the following estimation of total number of possible alloys:

$$N = 10^{58} \quad (2.2)$$

which is an enormous number of materials. Even if restricting to a five-component subspace and equiatomic composition, the total number of alloys still remains enormous:

$$N = 30^5 \quad (2.3)$$

To explore this huge chemical space conceptually new approaches, going beyond conventional alloying, are required. One of the recently developed alloying methods implies mixing multiple components (usually five or more) in high concentration.

However, apart from traditional melting and casting, this approach requires alternative synthesis techniques. This is especially important, when dealing with elements with a wide range of evaporation temperatures. For example, lighter elements may evaporate before the heavier have melted, which results in the reduction of concentration of lighter elements in a final compound [Svensson \[2015\]](#), [Maritsa et al. \[2022\]](#). In this case mechanical alloying techniques, for example, are considered as an alternative [Hammond et al. \[2014\]](#), [Stasiak et al. \[2023\]](#), [Rudolf Kanyane et al. \[2019\]](#).

2.2 High-entropy alloys

The new alloying method stimulated the discovery of conceptually new class of multicomponent materials with attractive mechanical and refractory properties. Their key feature consisted in presence of a high configurational entropy, caused by mixing of multiple components in approximately equal proportions. These materials coined a term “high-entropy alloys”, underlining the dominant role of a high mixing entropy in formation of these compounds. The pioneering work in investigation of these materials was performed by B. Cantor, who found that $\text{Co}_{20}\text{Cr}_{20}\text{Fe}_{20}\text{Mn}_{20}\text{Ni}_{20}$ forms a single fcc phase, i.e. all elements are mixed into a solid solution [Cantor et al. \[2004\]](#). Later, [Yeh et al. \[2004\]](#) proposed a theoretical justification of this phenomenon and introduced the term “high-entropy alloy”.

According to the hypothesis proposed by [Yeh et al. \[2004\]](#), the presence of multiple components in approximately equal proportions would cause mixing entropy to dominate over the enthalpy of formation and, thereby, contribute to the formation of an ideal solid solution instead of potentially brittle intermetallic phases (Fig. 2-1). The rationale behind this assumption is based on a change of Gibbs free energy when multiple components are mixed together. The Gibbs free energy change in the cases of formation of intermetallics and an ideal solid solution can be defined as follows:

$$\Delta G_f = \Delta H_f - T\Delta S_f \quad (2.4)$$

$$\Delta G_{\text{mix}} = \Delta H_{\text{mix}} - T\Delta S_{\text{mix}} \quad (2.5)$$

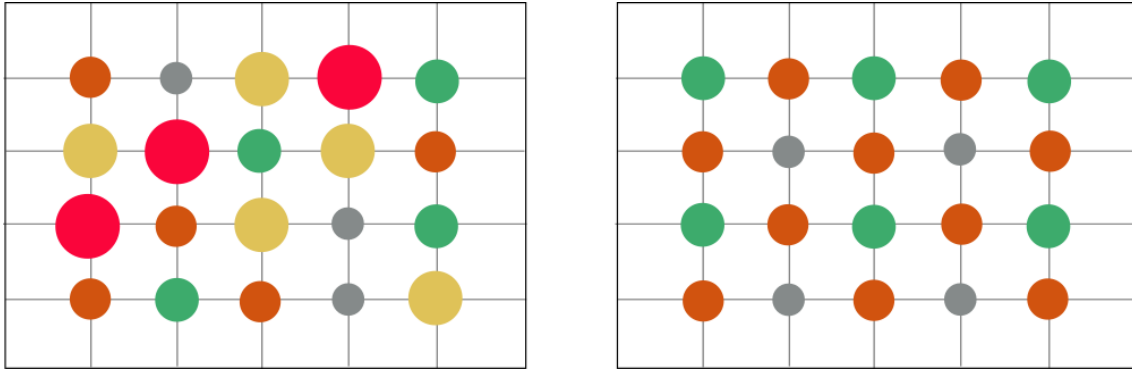


Figure 2-1: Schematic illustration of phases, which may form in HEA. Left - an ideal solid solution; right - ordered intermetallic phase.

where ΔG_f , ΔH_f , ΔS_f are the Gibbs free energy change, enthalpy and entropy of formation of an intermetallic compound; ΔG_{mix} , ΔH_{mix} , ΔS_{mix} are the Gibbs free energy change, enthalpy and entropy of mixing of an ideal solid solution. At the same time, the entropy of mixing is given by:

$$\Delta S_{\text{mix}} = R \ln n \quad (2.6)$$

where n is the number of chemical components in the alloy. Thus, when five and more elements are mixed together the values for ΔS_{mix} are exceeding $1.5R$. Based on this, Yeh and co-workers concluded that at high temperatures ($-T\Delta S_{\text{mix}}$) term becomes more negative than ΔH_f , thereby promoting formation of an ideal solid solution in favour of intermetallic phase. Initially, they attributed the term “high-entropy alloy” to compounds containing five or more chemical elements in nearly equiatomic concentrations. However, it has been proven that alloys with three principal elements, such as VCoNi, can also have high entropy [Sohn et al. \[2020\]](#). Additionally, the entropy factor starts playing a significant role in formation of a single phase even when $\Delta S_{\text{mix}} > 1R$. To classify materials with $1R < \Delta S_{\text{mix}} < 1.5R$ a term “medium-entropy alloy” (MEA) was introduced [Hong et al. \[2020\]](#).

Apart from high mixing entropy, three other core effects, contributing to excellent mechanical properties of HEAs, are reported in the literature. Namely, sluggish diffusion, lattice distortion and the cocktail effect.

The reason for slower diffusion rates in HEAs is quite straightforward. When

an atom diffuses in a lattice of a solid solution, it is quite unlikely that a local environment of this atom will remain similar along the transition path. On the contrary, chemical environments in two neighboring spots differ significantly and, hence, the potential energy should be also different. When potential energy in a neighboring spot is higher, diffusion is prevented. This case was analyzed in CoCrFeMnNi high-entropy alloy, where high fluctuations of lattice potential energy contributed to higher activation energies and, therefore, sluggish diffusion [Tsai et al. \[2013\]](#).

Lattice distortions are caused by a presence of elements with a high difference in atomic radii. Distortions are expected to hinder dislocation movement and contribute to a strengthening of a solid solution. However, in HEAs containing lighter elements, strengthening is barely caused by lattice distortions. For example, investigation of lattice distortions in pure Ni, CrNi, CoCrNi and CoCrFeMnNi revealed that the magnitude of lattice strain in these alloys is similar to that of pure Ni [Owen et al. \[2017\]](#). However, it becomes larger in CoCrFeNiPd due to larger atomic radii of Pd [Tong et al. \[2017\]](#). Recently, relevance of lattice distortions was questioned due to confounding effect of thermal vibrations on the diffraction peak intensity [Pickering and Jones \[2016\]](#). Nevertheless, in case of larger elements, alloy strengthening due to lattice distortions is likely the case.

The cocktail effect is usually mentioned to underline that properties of HEAs can't be considered as a superposition of properties of each constituent component. Instead, they originate from an interplay of the mentioned effects, such as lattice distortion, interaction of different elements and phases, etc.

Even though formation of intermetallic or complex phases is damped by the high configurational entropy, they are still possible. Different criteria were developed to predict formation of a solid solution phase in HEAs. Many of them are based on evaluation of configurational entropy and enthalpy of mixing. One rather successful criteria was given by [Yang and Zhang \[2012\]](#) and is based on evaluation of entropy-to-enthalpy ratio:

$$\Omega = \frac{T_m \Delta S_{\text{mix}}}{\Delta H_{\text{mix}}} \quad (2.7)$$

where T_m is the weighted average melting temperature of the constituent elements.

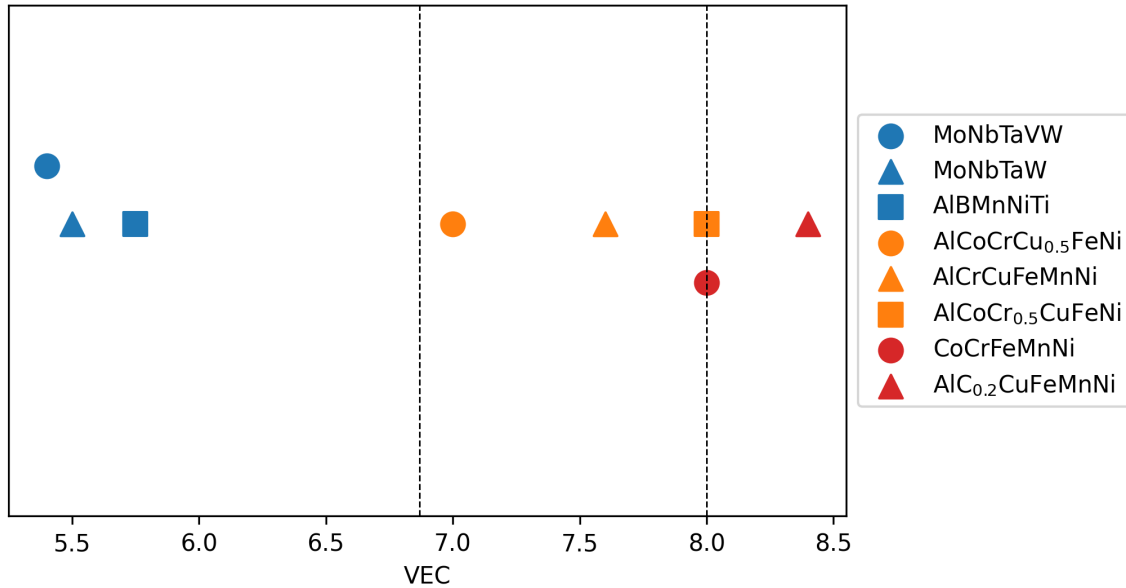


Figure 2-2: Dependence between VEC and phase stability in several HEAs. Blue symbols represent compounds with pure bcc phases; orange - a mixture of bcc and fcc phases; red - compounds with pure fcc phases.

As such, disordered phases are expected to form when $\Omega > 1.1$. Additionally, some studies were done in order to formulate criteria for predicting lattice type of a final compound. In work by Guo et al. [2011] a dependence between phase stability and valence electron concentration (VEC) was investigated. They observed that for $VEC < 6.87$ bcc phase was stable, while fcc phase was stable when $VEC \geq 8$. This trend can be observed on Fig. 2-2, where dependence between VEC and phase stability is presented for some HEAs.

2.3 Computational materials modeling

Efficient sampling of multicomponent phase space, even restricted to HEAs, is rather impractical with an experimental approach. This is caused by an enormous number of all possible chemical combinations (see equations 2.1 - 2.3). To overcome this barrier, computational materials modeling methods are widely used in the study of multicomponent materials. They are used to investigate materials at different levels of theory, ranging from their electronic structure to microstructure. Depending on the level of treatment, these methods differ in their computational complexity

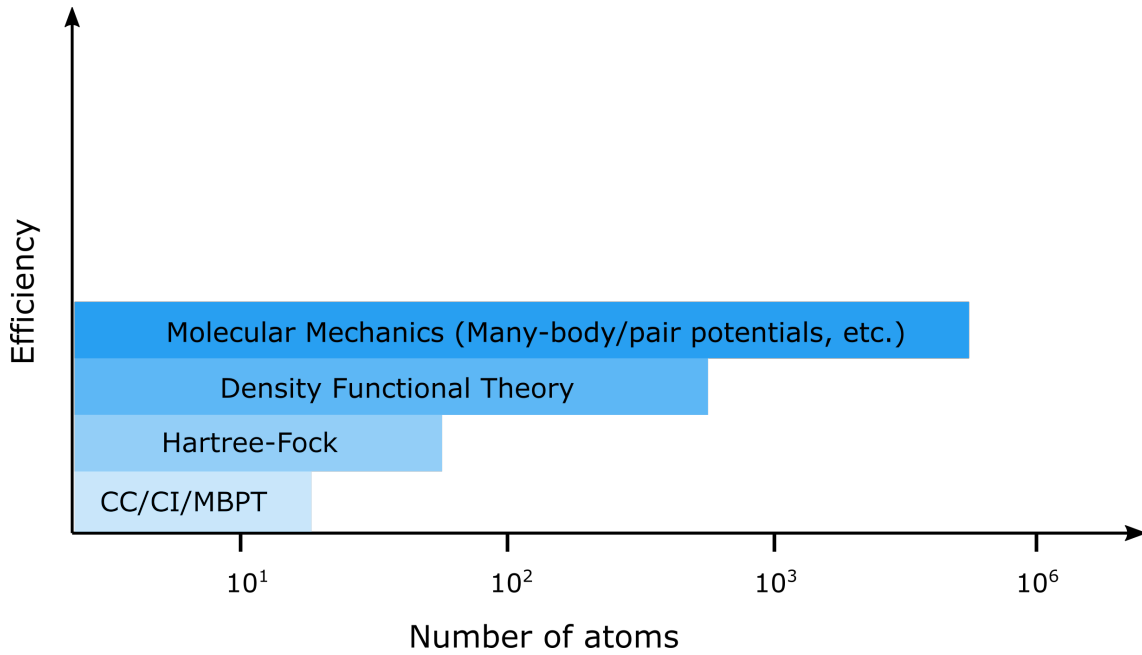


Figure 2-3: Efficiency of atomic interaction approximation methods with corresponding scales of the simulated system.

and accuracy. Electronic structure methods are the most accurate at the expense of computational efficiency. They allow to investigate various phenomena, originating on a quantum level, such as electron transport, formation of electronic bands, etc. Microstructural analysis can be performed using methods with a higher degree of approximation. They require fewer computational resources and, hence, are useful in simulations of materials at scales comparable to experiment. For example, these methods can be used to study crack propagation [Lee et al. \[2023\]](#), [Stepanova and Bronnikov \[2019\]](#), dislocation or grain boundary movements in polycrystalline materials [Hodapp et al. \[2018\]](#), [Grabowski and Zotov \[2021\]](#).

Electronic structure methods are a part of an *ab initio* class of methods. They do not require any empirical parameters and are based solely on solution of many-particle Schrödinger equation, which describe interaction of atoms and electrons. Since interaction itself is complex in its nature, several approximations were introduced to reduce complexity of the problem. The foundational principle behind all electronic structure methods is Born-Oppenheimer approximation [Bechstedt \[2015\]](#). It implies that electrons are moving in an external field, created by immovable nuclei. This assumption sufficiently reduces the number of variables in many-particle

wave function. The second ingredient consists in approximating a wave function, accounting for physical aspects peculiar to fermionic systems. One example is the Slater determinant [Jensen \[2007a\]](#), which satisfies anti-symmetry and consequently Pauli exclusion principle. It is used in Hartree-Fock (HF) method [Valatin \[1961\]](#) to determine the ground state energy of an atomic system. However, the HF method lacks electron correlation, which is very important in describing interactions precisely. To account for electron correlation, methods like configuration interaction (CI), coupled cluster (CC) or many-body perturbation theory (MBPT) were developed [Jensen \[2007b\]](#). The listed methods belong to a class of wave function methods, which are the most accurate in describing chemical phenomena. However, due to dimensionality problem, their efficiency falls dramatically when size of the system is increased. This is explicitly shown on [Fig. 2-3](#), where dependence between system size and applicability of an approximation method is shown. A conceptually separate method, known as density functional theory (DFT) [Jensen \[2007c\]](#), was introduced to overcome dimensionality issues. Due to efficient approximations introduced in DFT the method has been widely used for more than two decades in the study of various chemical systems.

In more approximate methods, as a rule, quantum effects are neglected and atoms are considered as classical objects. The common example is molecular mechanics, which is based on force-fields, or in case of solid state systems, interatomic potentials [Jensen \[2007d\]](#). These potentials are represented by functions of pair or many-body interactions. As classical models they account for mechanical deformation of bonds like stretching, bending or torsional movement, although, some approximation of quantum effects like electrostatic interaction can be also included. Their main advantage in comparison to electronic structure methods consists in computational efficiency. As shown on [Fig.2-3](#), molecular mechanics allow to simulate systems with up to 10^6 atoms, while the size of the systems that can be studied with DFT is three orders of magnitude less. Nevertheless, DFT was extensively used in this work to obtain accurate approximation models of interatomic interaction. The further introduction to the used methods will start with the description of DFT.

2.3.1 Density functional theory

Density functional theory is a quantum mechanical method to calculate an approximate electronic structure of an atomic system. The method is built upon two main postulates. The first comes from Born-Oppenheimer approximation, described in section two. The second is based on the fact that properties of a fermionic system are determined by an electron density. Hence, the number of variables in Schrödinger equation are reduced from $3N$ to only three.

The theoretical foundation of DFT is formulated in the Kohn-Hohenberg theorems. The first theorem states that ground state energy from the Schrödinger equation is a unique electron density functional [Jensen \[2007c\]](#). The second theorem states that the electron density, corresponding to the minimum of energy functional, is the true electron density corresponding to the exact solution of the Schrödinger equation [Jensen \[2007c\]](#). Additionally, an explicit electron correlation is neglected and, hence, the Schrödinger equation is solved for a system of effectively non-interacting electrons. The reformulated equations are called Kohn-Sham equations [Sham and Kohn \[1966\]](#) and are given as follows:

$$\left[\frac{\hbar^2}{2m} \nabla^2 + v_{\text{eff}}(\mathbf{r}) \right] \psi_i(\mathbf{r}) = \epsilon_i \psi_i(\mathbf{r}) \quad (2.8)$$

where ϵ_i is the orbital energy of the corresponding Kohn-Sham orbital ψ_i and the density of N -particle system is

$$n(\mathbf{r}) = \sum_i^N |\psi_i(\mathbf{r})|^2. \quad (2.9)$$

The last term in 2.8 $v_{\text{eff}}(\mathbf{r})$ is a Kohn-Sham potential given as:

$$v_{\text{eff}}(\mathbf{r}) = v_{\text{ext}}(\mathbf{r}) + e^2 \int \frac{n(\mathbf{r}')}{|\mathbf{r} - \mathbf{r}'|} d\mathbf{r}' + \frac{\delta E_{\text{XC}}[n]}{\delta n(\mathbf{r})} \quad (2.10)$$

where $v_{\text{ext}}(\mathbf{r})$ is electron-nuclear interaction, the second term is the Hartree potential, and $\frac{\delta E_{\text{XC}}[\rho]}{\delta \rho(\mathbf{r})}$ is an exchange correlation potential. The latter term is the only unknown in Kohn-Sham DFT and is added to account for an electron correlation.

Similar to the Hartree-Fock equation 2.8 is solved in a self-consistent fashion. The procedure is given by the following steps:

1. Set trial electron density $n(\mathbf{r})$
2. Solve equation 2.8 using trial $n(\mathbf{r})$ to obtain Kohn-Sham orbitals ψ_i and corresponding orbital energies ϵ_i
3. Evaluate new electron density as $n_{\text{KS}}(\mathbf{r}) = 2 \sum_i \psi_i^*(\mathbf{r})\psi_i(\mathbf{r})$
4. If $n_{\text{KS}}(\mathbf{r}) \approx n(\mathbf{r})$ then the ground state of the system is found. Otherwise, self-consistent loop continues.

One of the main problems in Kohn-Sham DFT is the choice of the exchange correlation functional. Many variants have been developed to date and the most common among them are local density approximation (LDA) and generalized gradient approximation (GGA) Jensen [2007c]. In LDA the exchange correlation energy is given as:

$$E_{\text{XC}}^{\text{LDA}}[\rho] = \int n(\mathbf{r})\epsilon_{\text{XC}}(n(\mathbf{r}))d\mathbf{r}, \quad (2.11)$$

where $\rho(\mathbf{r})$ is the electron density and ϵ_{XC} is the exchange-correlation energy per particle. The LDA is based on the assumption that the electron density locally can be treated as a uniform electron gas. This gives an underestimation of an exchange-correlation energy and, hence, lead to inaccurate results for some chemical systems. The non-homogeneity of the true electron density is taken into account in GGA functionals. Specifically, an exchange-correlation integral is expanded with the gradient of the electron density:

$$E_{\text{XC}}^{\text{GGA}}[\rho] = \int n(\mathbf{r})\epsilon_{\text{XC}}(n(\mathbf{r}), \nabla n(\mathbf{r}))d\mathbf{r}. \quad (2.12)$$

An account for electron density gradient make GGA more robust in describing materials with different types of bondings. In comparison with LDA, GGA's tend to improve total and atomization energies Perdew et al. [1992], Constantin et al. [2011], as well as structural energy differences Hammer et al. [1993], Hamann [1996]. In

this work GGA functional was used for an accurate calculation of total ground-state energies of multicomponent alloys.

Nevertheless, DFT is very restrictive in the study of large systems: computational costs have a polynomial dependence on a size of a simulation cell ($\approx N^3$ for DFT, where N is the number of particles). This imposes constraints on the study of key properties of multicomponent materials such as phase stability, mechanical resistance as well as prohibits high-throughput search in multicomponent chemical space. For that reason, approximating models, allowing for simulating systems with a large number of atoms ($N \gg 200$) at accuracy comparable to DFT, are being actively developed. These models, known as interatomic potentials, are discussed further.

2.3.2 Empirical potentials

Empirical potentials are historically the first example of surrogate interatomic interaction models. They had quite restricted applicability range, and required experimental parameters in their functional form. In general, it resembles the physical principles of interatomic interaction, as it accounts for bond stretching, bending, torsional movement and electrostatic interaction. In these models, atoms are treated as classical objects and any effects of quantum origin, such as electrostatic interaction, are represented by empirical parameters. For that reason, their computational efficiency is much higher than that of *ab initio* methods. One example of this class of models is the Tersoff potential. It is used to describe silicon and Si-based compounds, such as SiO₂. For metallic systems, the most common potential is embedded atom model (EAM) [Deye et al. \[Mar 2013\]](#). Its functional form is given as follows:

$$E_i = F_\alpha\left(\sum_{j \neq i} \rho_\beta(r_{ij})\right) + \frac{1}{2} \sum_{j \neq i} \phi_{\alpha\beta}(r_{ij}) \quad (2.13)$$

where E_i is the potential energy of atom i ; r_{ij} is the distance between atoms i and j ; $\phi_{\alpha\beta}$ is the pair-wise potential function of atoms with types α and β ; ρ_β is the contribution to electron density from atom j of type β at the location of atom i of type α ; F_α is the embedding function, representing the energy required to place

atom i of type α into the electron cloud. Embedded atom model works efficiently for single component and binary systems, but their application to multicomponent materials is restricted. Thus, to describe interactions in a single component system three functions are needed to be set: two embedding functions and one pair-wise interaction function. For two components the number of required functions is seven. Therefore, computational efficiency of the model falls down with the increase of chemical elements in the system, since more *ab initio* calculations are needed to set these parameters. To overcome this issue non-parametric potentials are being actively developed. Usually, they do not require any physical parameters and their accuracy depends on the quality of data obtained from *ab initio* calculations.

2.3.3 Machine-learning interatomic potentials

Though the functional form of empirical potentials provides high computational efficiency, they have a number of sufficient limitations in modeling multicomponent materials. Apart from a large number of *ab initio* calculations, required to set the parameters for a multicomponent system, parametric potentials are loosely transferable between different chemical systems. For example, in embedded atom model it is assumed that the atom experiences the interaction of a local electron gas. This assumption approximates the physical nature of metallic bonding, which limits application of EAM to metallic systems. To overcome limited transferability and other aforementioned issues, a conceptually new class of potentials, namely non-parametric potentials, are being actively developed.

In general, functional form of non-parametric potentials do not resemble any physical nature of interatomic interaction. Instead, it is represented by interpolative models that fit the data, obtained from *ab initio* calculations as it is shown on Fig.2-4. Ability of these models to yield physically meaningful results is based on data mining. Hence, transferability of non-parametric potentials between different systems can be achieved by providing relevant chemical data. Accuracy of non-parametric potentials largely depends on the type of *ab initio* data they are fitted to. Thus, models fitted to DFT calculations can reproduce results of a comparable accuracy using much less computational costs.

In modern atomistic simulations non-parametric potentials are mainly represented by machine-learning methods. One of the first examples were artificial neural network based potentials proposed by Behler and Parrinello (BPNN) [Behler and Parrinello \[2007\]](#). They use an artificial neural network (ANN) as a regressor to map atomic configuration to their energies. Despite the absence of any physical parameters in the functional form, ANN should preserve the symmetries of an atomic configuration, i.e, predicted energy should be invariant under any spatial transformation of a structure. To fulfill this condition, they proposed partitioning total configurational energy into a sum of energy contributions of local atomic neighborhoods of each atom. Hence, the total energy is given as follows:

$$E_{\text{tot}} = \sum_i V(n_i) \quad (2.14)$$

where $V(n_i)$ is the energy contribution of atomic neighborhood n_i of atom i . This approach was implemented by using a set of subnets, where each of them is mapping local atomic neighborhoods to corresponding energy contributions.

Further, an energy partitioning approach was implemented in other machine-learning interatomic potentials. One of the recent examples are moment tensor potentials (MTPs), proposed by A. Shapeev [Shapeev \[2016\]](#). Unlike BPNN, MTP employs linear regression and the atomistic system is represented with invariant polynomials. The energy contribution of an atomic environment is expanded through a set of basis functions B_α :

$$V(n) = \sum_\alpha \xi_\alpha B_\alpha(n) \quad (2.15)$$

where $B_\alpha(n)$ enumerate all possible contractions of moment tensor descriptors, given as follows:

$$M_{\mu,\nu}(n_i) = \sum_j f_\mu(|r_{ij}|, z_i, z_j) \underbrace{r_{ij} \otimes \dots \otimes r_{ij}}_{\nu \text{ times}} \quad (2.16)$$

where the index j enumerates all atoms in the environment n_i of atom i ; f_μ is the radial distribution function; r_{ij} is the distance between atoms i and j ; z_i and z_j are chemical types of atoms i and j . Functions $B_\alpha(n)$ are invariant with respect to translations, rotations and reflections of the atomic neighborhood. Hence, $V(n)$

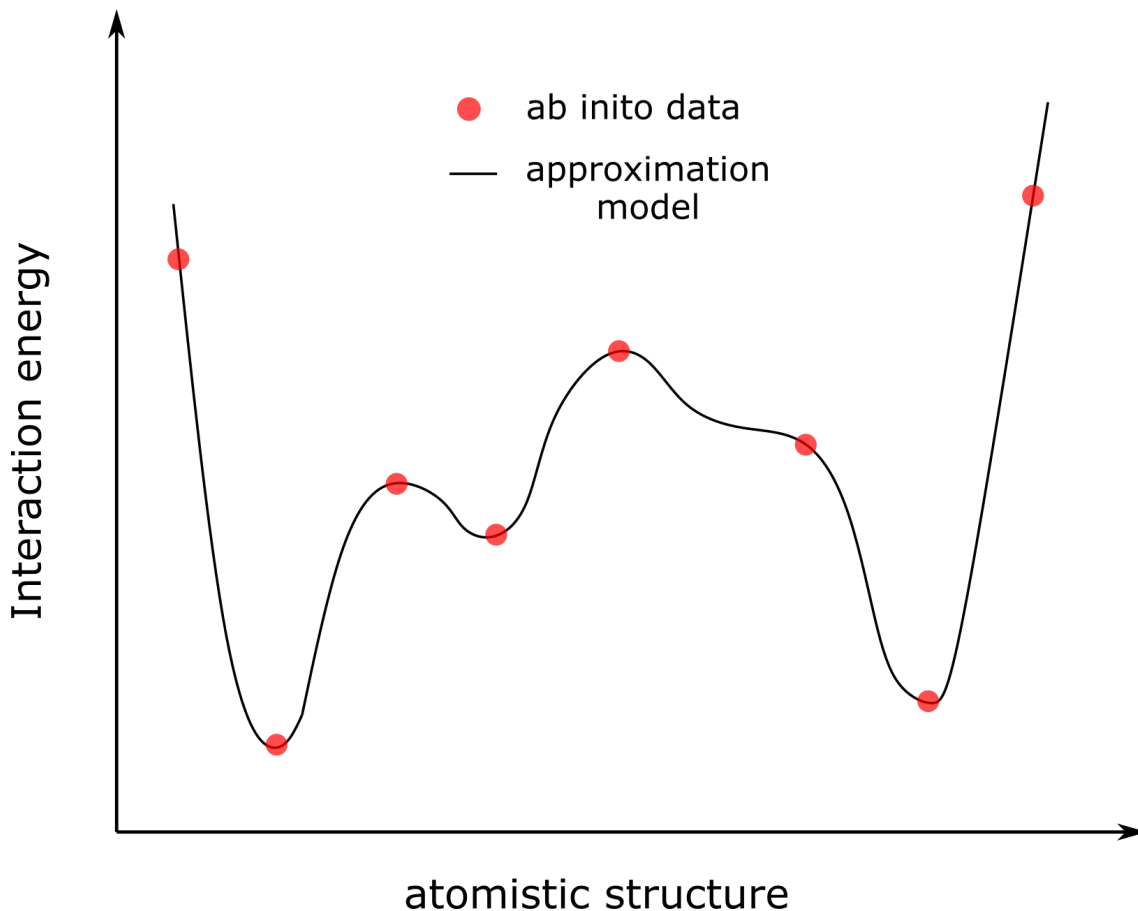


Figure 2-4: Illustration of an idea of fitting to *ab initio* data. Red markers correspond to calculated data (structure/energy), black line illustrates the fitting model.

also preserve these symmetries. Over the last few years a sufficient improvement of MTP was done, including an active learning algorithm [Gubaev et al. \[2019\]](#), and extension which explicitly accounts for magnetic degrees of freedom [Novikov et al. \[2021\]](#).

Moment tensor potentials can be used as interatomic interaction model in a wide range of simulations including molecular dynamics, “off-lattice” Monte-Carlo and crystal structure prediction methods such as USPEX. These potentials has been successfully applied to prediction of new boron allotropes [Podryabinkin et al. \[2019\]](#), as well as several stable compositions of Al-Ni-Ti system [Gubaev et al. \[2019\]](#); study of magnetic properties of materials [Novikov et al. \[2021\]](#) and investigation of thermal conductivity [Mortazavi et al. \[2020a,b, 2021\]](#).

Both MTP and BPNN account for spatial degrees of freedom, i.e. atomic positions are adjusted during the simulations. This puts significant constraints on the

study of multicomponent materials (with four or more chemical components) using these potentials, since the configurational space increases enormously. For that reason simpler models have been developed recently. They account only for the chemical types of atoms and the simulation is performed on a pre-defined crystal structure. For that reason they are called “on-lattice” models. One example is the LRP, proposed by A. Shapeev [Shapeev \[2017\]](#). Being an “on-lattice” model, LRP has a fixed geometry of an atomic neighborhood and the corresponding energy contribution depends only on the local chemical order around the central site of the neighborhood. Unlike MTP and BPNN, LRP does not have a distinctive functional form. The potential itself is represented in a form of a multidimensional tensor, whose parameters are obtained from fitting to DFT calculations.

Another “on-lattice” model, which is also based on data mining, though not considered as a machine-learning method, is cluster expansion (CE) [Sanchez \[2010\]](#). Unlike in aforementioned potentials, total configurational energy is partitioned into energy contribution of atomic clusters, represented by pairs of atoms, triplets, etc. Parameters of this model are called effective cluster interactions (ECI) and are fitted from DFT calculations. Cluster expansion has been applied to study a number of multicomponent systems, including quaternary Nb-Mo-Ta-W and quinary Nb-Mo-Ta-V-W [Widom \[2016, 2018\]](#). However, the number of fitting parameters of CE model increases more rapidly than that of LRP, when the number of chemical components is increased, as discussed further in the text. This makes the latter a more preferable choice in the study of multicomponent materials. Both CE and LRP were employed in the present work and their details are discussed further.

2.3.4 Cluster expansion

In cluster expansion model [Sanchez \[2010\]](#) the energy contribution of an atomic neighborhood is calculated as follows:

$$V(\sigma_1, \dots, \sigma_n) = \sum_{ij} J_{ij} \sigma_i \sigma_j + \sum_{ijk} J_{ijk} \sigma_i \sigma_j \sigma_k + \dots, \quad (2.17)$$

where $J_{i,j}$ and $J_{i,j,k}$ are the so-called effective cluster interactions (ECIs) of pair and triplet atomic clusters of the neighborhood; σ_i , σ_j and σ_k are types of atoms i , j and k . Total configurational energy is then calculated as it was described in Eq.2.19.

The ECIs are obtained by minimizing the mean-squared error functional:

$$\frac{1}{K} \sum_{k=1}^K |E(\sigma^{(k)}) - E^{qm}(\sigma^{(k)})|^2, \quad (2.18)$$

where $\sigma^{(k)}$ denotes atomic configurations, K is the size of the training set, and $E(\sigma^{(k)})$ and $E^{qm}(\sigma^{(k)})$ are the energies of $\sigma^{(k)}$ calculated by the CE and DFT, respectively. The minimization is done using ordinary least squares method. In this work the CE model is used to evaluate energies of binary and ternary configurations during on-lattice CSP modeling. However, as will be reasoned further, energies of structures with more chemical components are evaluated using LRP.

2.3.5 On-lattice low-rank potential

Developing an accurate non-parametric potential for multicomponent alloys is a non-trivial task. The main problem consists in a combinatorial growth of the number of fitting parameters as the number of chemical components in the system increases. For example, let's estimate the number of ECIs in a CE model with three types of clusters: pair of nearest neighbours, triple cluster and a cluster of four atoms. The number of ECIs for a particular cluster can be estimated as m^n (where m is the number of chemical components, n - number of atoms in the cluster). Thus, such CE model will have $3^2 + 3^3 + 3^4 = 117$, $4^2 + 4^3 + 4^4 = 336$, $5^2 + 5^3 + 5^4 = 775$ ECIs for ternary, quaternary and quinary systems respectively. The number of ECIs can be truncated, but this requires additional techniques such as compressed sensing [Nelson et al. \[2013\]](#), that, on practice, do not sufficiently reduce the amount of required *ab initio* data in case of multicomponent systems. Hence, this model requires an additional improvement.

The solution, proposed recently by A. Shapeev, consists in representing a fixed-lattice interaction model in a tensor-train format [Shapeev \[2017\]](#). The proposed model was named the low-rank potential (LRP). Similarly to CE, an atomic struc-

ture in the LRP model is represented by an ideal crystalline lattice, where each site corresponds to an atom of a certain chemical type. The sequence of chemical types of atoms, surrounding any atom of the crystalline lattice is called the neighborhood of this atom. This sequence is given by a collection of neighbors of a chosen site on a defined crystalline lattice. Usually, the atomic neighborhood is formed of the atoms occupying nearest neighboring sites. Thus, in a bcc lattice the neighborhood consists of 9 atoms, while in a fcc lattice 13 atoms form the neighborhood (including the central atom in bcc and fcc). However, in case of bcc it is common to include second nearest neighbors (i.e., 15 atoms in total). The LRP model can be represented as a multidimensional tensor of size m^n (m - number of chemical types, n - size of the chemical environment), where each element correspond to an energy contribution from the unique atomic neighborhood. The total configurational energy, therefore, can be calculated as a sum of energy contribution of each environment:

$$E(\sigma) = \sum_{\xi \in \Omega} V(\xi) \quad (2.19)$$

where Ω are lattice sites, periodically repeated in space, and ξ is central atoms of atomic environments.

The LRP model employs a tensor-train (TT) decomposition to obtain its parameters [Oseledets \[2011\]](#). This method consists in finding a set of matrices of size r whose product restores the elements of the original tensor. The energy of an atomic neighborhood in a tensor-train format is given as following:

$$V(\sigma_1, \dots, \sigma_n) = \prod_i A_i(\sigma_i), \quad (2.20)$$

where A_i are the matrices of the tensor-train representation and σ_i are the types of atoms in the neighborhood. The sizes of A_1, A_n are $1 \times r$ and $r \times 1$, and A_2, A_{n-1} have the size $r \times r$, where r is also called as the rank of decomposition. Eventually, the product in Eq. 2.20 yields a scalar. By using a tensor-train decomposition method, the number of parameters are reduced from m^n to nmr^2 . Thus, for a five component alloy with a bcc lattice, upon applying a decomposition with a

rank $r = 5$, the number of parameters are reduced from $m^n = 5^9 = 1953125$ to $nmr^2 = 9 \cdot 5 \cdot 5^2 = 1125$. The parameters are obtained by minimizing the following functional:

$$\frac{1}{K} \sum_{k=1}^K |E(\sigma^{(k)}) - E^{qm}(\sigma^{(k)})|^2, \quad (2.21)$$

where $\sigma^{(k)}$ denotes atomic configurations, K is the size of the training set, and $E(\sigma^{(k)})$ and $E^{qm}(\sigma^{(k)})$ are the energies of $\sigma^{(k)}$ calculated by LRP and DFT, respectively. The minimization is done by the alternating least squares method (ALS), which optimizes one matrix A_i at a time, and simulated annealing that adds random Gaussian noise to every element of A_i , which decreases from one ALS iteration to the next one.

2.4 Structure generation methods

An integral part of computational materials modeling are structure generation methods. In combination with energy evaluation models they provide mechanically stable configuration with minimum potential energy. Structure generation algorithms are used in a number of simulations, including study of diffusion processes, structural relaxation or prediction of stable crystal structures. When initial configuration is close to an energy minimum a number of well-established optimization methods can be applied. Among them are, for example, conjugate gradient (CG), Newton-Raphson, quasi-Newton, truncated Newton [Nocedal and Wright \[2006\]](#), [Press et al. \[1992\]](#) and variants of molecular dynamics [Schlick \[2002\]](#), [Hagelaar et al. \[2006\]](#). When initial geometry is far from the optimal, local optimization methods become computationally inefficient. In this case random walk approaches are more reasonable for sampling PES. One example, widely used in materials simulations, is Markov Chain Monte Carlo (MCMC), based on Metropolis-Hastings algorithm [Robert and Casella \[1970\]](#). Its principle is based on the simulated annealing with acceptance/rejection of best/worst random moves on PES. These simulations can be accelerated even further with the use of non-parametric potentials for energy evaluation. Given this a faster convergence to a global minimum can be provided.

Nevertheless, structural optimization of multicomponent materials still remains computationally complex due to a huge size of configurational space. Probing all possible atomic configurations is a combinatorially difficult task. However, for metallic alloys the problem can be significantly simplified. The structure of these materials is described by common lattices such as bcc, fcc or HCP within a wide temperature window. Hence, the optimal geometry is already known and the structural optimization can be reduced to finding lattice decorations (i.e., the way how atoms occupy sites of the fixed lattice) corresponding to the lowest energy. This lattice-based approach, also known as “on-lattice”, has been widely used in Monte Carlo simulations to study phase stability of multicomponent alloys. Among the recent examples are equimolar Nb-Mo-Ta-W Widom [2016], Kostiuchenko et al. [2019], Cr-Mo-Nb-W Widom [2016] and V-Co-Ni Kostiuchenko et al. [2020], to name a few. In this work it was demonstrated that on-lattice Monte Carlo can be applied to investigate a wider range of physical phenomena. Among them are phase stability of high-entropy carbides and contribution of magnetism to the short-range order in medium-entropy alloys.

Another problem in materials design, that require a more sophisticated structure generation method, is crystal structure prediction. An effective solution, proposed recently, is based on evolutionary algorithms. One of the most successful examples is USPEX Glass et al. [2006]. This method operates with population of configurations, discarding the worst and selecting the best as “parents” for a next generation. The structures are selected based on their thermodynamic potential evaluated with *ab initio* calculations. Population of new structures is produced using one of the three operators: (i) heredity, which combines slabs of two parent structures; (ii) permutation, which swaps atoms of different chemical types; (iii) lattice mutation, which distorts the shape of the cell. After, the produced structures are locally optimized. A significant number of materials with wide range of properties and chemical composition were discovered with USPEX Dong et al. [2019b, 2018], Yao et al. [2018]. The overall number of reported works, utilizing this method, exceeds several hundred and the method is still being actively developed.

Crystal structure prediction can be also optimized with the “on-lattice” approach.

One of the first examples, solving the CSP problem in a lattice-based fashion, was an algorithm developed by [Hart and Forcade \[2008, 2009\]](#). It consisted of two steps: (1) generation of unique unit cells on a defined crystal lattice and (2) generation of unique lattice decorations within those cells. Step 1 was accomplished by representing each unit cell in Hermite Normal Form and eliminating the identical ones under rotations. The second step consisted in generation of all possible lattice decorations, excluding symmetrically equivalent. This method is simply the direct enumeration of all possible configurations. However, such approach would cause a combinatorial explosion when the size of the unit cell is increased. For that reason, an extension to the second step of the original algorithm was developed [Hart et al. \[2012\]](#). In the updated version, configurations only with a fixed concentrations were considered. Later the method was combined with the machine-learning potentials [Gubaev et al. \[2019\]](#), that accelerated the search by a factor of 100 to 1000. Still, the number of discovered structures was limited to a few hundred thousand which for the case of quaternary compounds corresponds to small unit cells, with at most nine atoms. In this work I propose a new lattice-based CSP method, called the on-lattice CSP [Sotskov et al. \[2023\]](#), that, as will be shown further, can discover multicomponent structures with larger unit cells and various chemical composition. The proposed algorithm is based on a principally new concept: instead of generating crystal structure prototypes as it is done in USPEX and the algorithm proposed by [Hart and Forcade \[2008\]](#), on-lattice CSP produces a crystal structure by consistently adding atom-by-atom to an empty configuration. Further it will be shown that this new approach is also effective in the discovery of new materials.

The working principle of the structure generation algorithms, presented in this work, is tied with machine learning potentials. Therefore, their description will be given along with the simulation methodology in the next section.

Chapter 3

Methodology of multicomponent alloys modeling

The technical novelty of this work consists in the development and application of on-lattice simulation tools to investigation of multicomponent alloys, namely crystal structure prediction and modeling of phase stability. For crystal structure prediction task a novel structure generation algorithm, called “on-lattice CSP”, was developed. Phase stability of high-entropy alloys was investigated using well-established on-lattice canonical Monte Carlo. However, the present work reveals the possibility of applying this method to investigation of materials with different chemistry, such as high-entropy carbides. The presented methodology was implemented in a stand-alone programming package (see Sec. 8.1). It contains implementation of all the mentioned structure generation algorithms as well as the CE and LRP potentials. Currently, the package can be used for modeling systems with bcc and fcc lattices as will be shown in the next chapters.

3.1 On-lattice CSP

On-lattice crystal structure prediction (on-lattice CSP) is a method for predicting stable crystal structures at 0 K. Generally, this can be done using canonical Monte Carlo at zero temperature. However, CMC is limited to configurations with a fixed concentration, while on-lattice CSP samples the complete compositional

space. Since the number of potentially stable structures with different compositions is enormously large (see Eq. 2.1 - 2.3), the algorithm was designed to sample the most prominent areas of the phase space.

To enforce importance sampling, the algorithm employs an evolutionary strategy. During each iteration the set of structures is produced among which the candidate with the lowest energy is chosen as a parent for the next generation. Unlike other structure generation algorithms, on-lattice CSP does not generate candidate structures with a complete unit cell. Instead, a configuration is "grown" atom by atom until the periodicity in the growing structure will be observed.

Structure growth procedure is presented on Fig. 3-1. As it is seen, the growth starts from an empty configuration. After that, one atom of each chemical type is added. This produces N candidate structures (two in binary case). On the next step the energies of all the produced structures are calculated and the one with the lowest energy is selected. Next, an atom of each chemical type is added to the selected structure and a population of new N candidates is produced. Their energies are calculated and the lowest energy structure is selected. This process continues further in the same way. Note that at this stage the "growing" configuration is not periodic (does not have a supercell) and it can be considered as the collection of individual atoms. Therefore, during this stage the growth do not follow any symmetry operations. The growth is guided only by an interatomic interaction model. The atoms are simply added in the sites of the lattice without accounting for translation, rotation or reflection symmetries.

Every time a new atom is added to the configuration, algorithm searches for two identical atomic neighborhoods. Once they are discovered, a unit cell vector is constructed by connecting the centers of these neighborhoods (Fig. 3-2a). After that, the growth area is reshaped using the constructed vector (Fig. 3-2b) and outer atoms are translated into the new growth area (3-2c). During this process "conflicting" atoms can appear. These are the atoms of different chemical types that share the same lattice site after the translation. In this case algorithm chooses an atom of the chemical type that results in a lower energy of a configuration (Fig. 3-2d-e).

After these steps the structure growth continues within a new area. Once a new

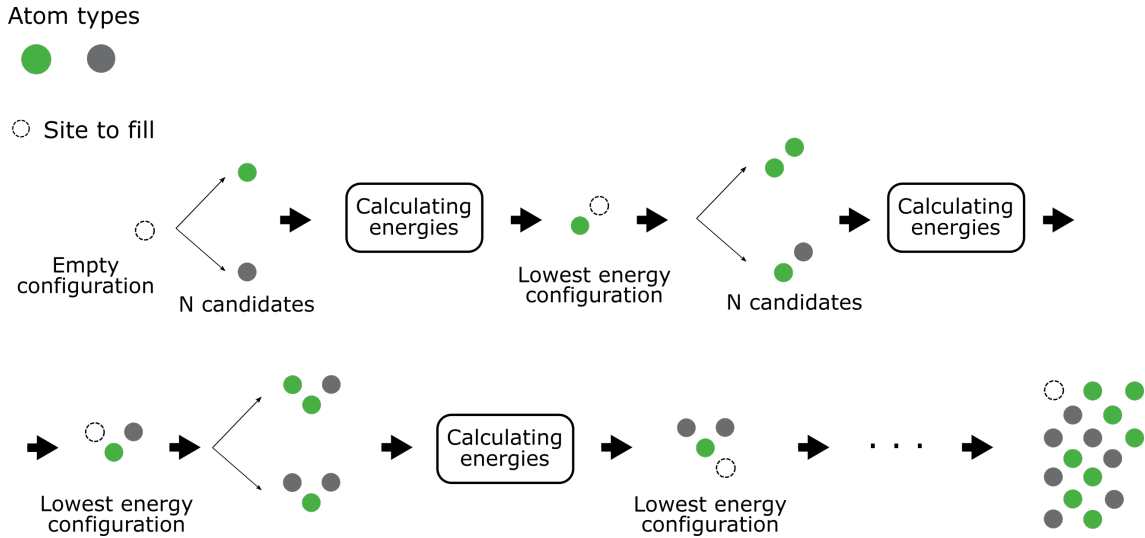


Figure 3-1: Illustration the structure “growth” process in on-lattice CSP.

pair of identical atomic neighborhoods is discovered, the second unit cell vector is constructed. As in the previous case, the growth area is reshaped with the second vector, atoms are translated inside and the conflicts are resolved. Finally, all the same steps are performed until the third vector is constructed. Once all three unit cell vectors are obtained the final structure is discovered (Fig.3-3).

During the structure growth stage, the added atoms have incomplete atomic neighborhoods. Such atoms create a substantially large surface with less number of pairwise interactions in comparison with the bulk. This, in turn, cause an increase in the interaction energy, and the algorithm might choose an undesired structure growth trajectory. To minimize this effect a strategy which I called the “alchemical” potential was applied. It consists in representing the energy of an incomplete neighborhood as an average of energies of all the alternative neighborhoods that can be created instead of the incomplete one. Thus, the energy of such neighborhood is calculated as:

$$V(\sigma_{\text{al}}) = \frac{V(\sigma_1) + \dots + V(\sigma_N)}{N} \quad (3.1)$$

where $V(\sigma_1), \dots, V(\sigma_n)$ are energies of the alternative neighborhoods, and N is the total number of such neighborhoods. The process of evaluating the energy of an “alchemical” neighborhood is illustrated on Fig. 3-4. The idea of averaging instead of choosing a lowest energy neighborhood comes from the fact that initially the

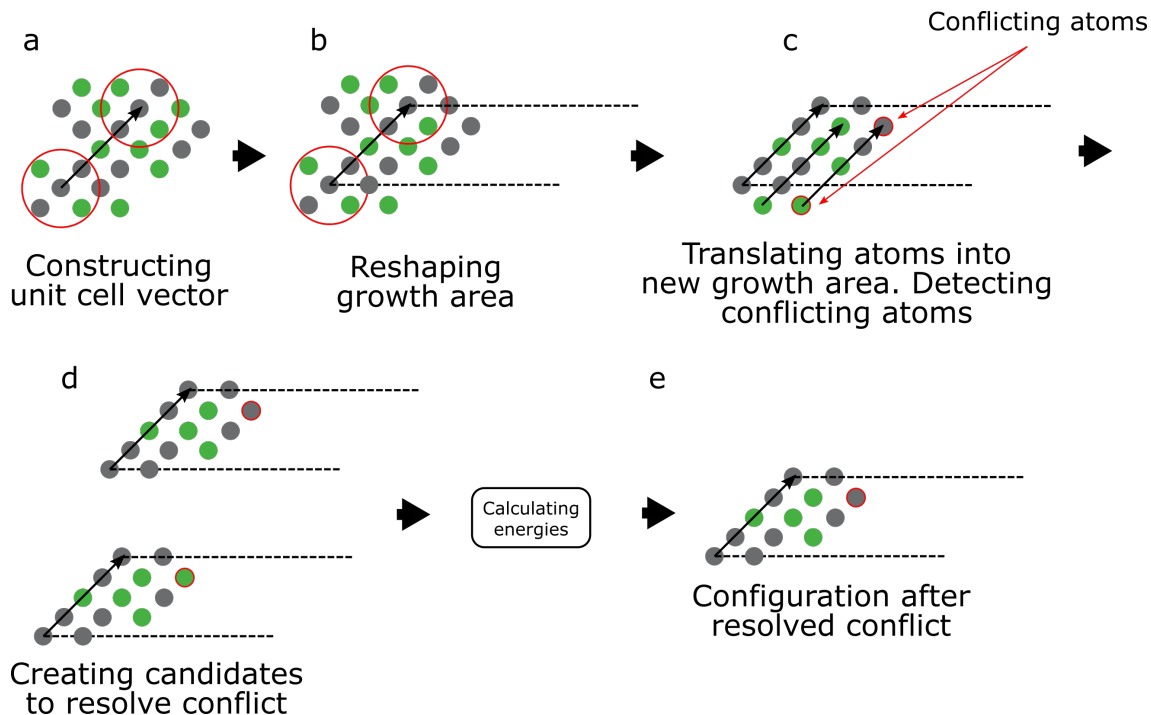


Figure 3-2: Construction of a first unit cell vector. Centers of identical neighborhoods are connected (a). The growth area is reshaped (b). Outer atoms are translated into a new growth area, conflicting atoms are detected (c). Resolving conflicts by choosing lowest energy configuration (d-e)

trajectory of a structure generation algorithm is unknown. The averaging allows one to minimize the possibility of missing the lowest energy structure without causing an abrupt change in growth trajectory, since during this process only one “real” atom is added. Choosing a lowest energy neighborhood instead might cause an opposite effect.

On-lattice CSP generates only one configuration during a single run. Hence, if the simulation is restarted with the same potential, the algorithm will discover the same configuration each time. To discover new structures, the potential is biased after each run. The biasing consists of adding a constant value δ to the energy contribution of each atomic neighborhood present in the discovered structure. Therefore, during the next run the previously discovered structure will have a higher energy and the algorithm will adopt a different structure generation path (if it happens that the same path is chosen, the resulting structure will be biased again until the biasing will result in the new structure).

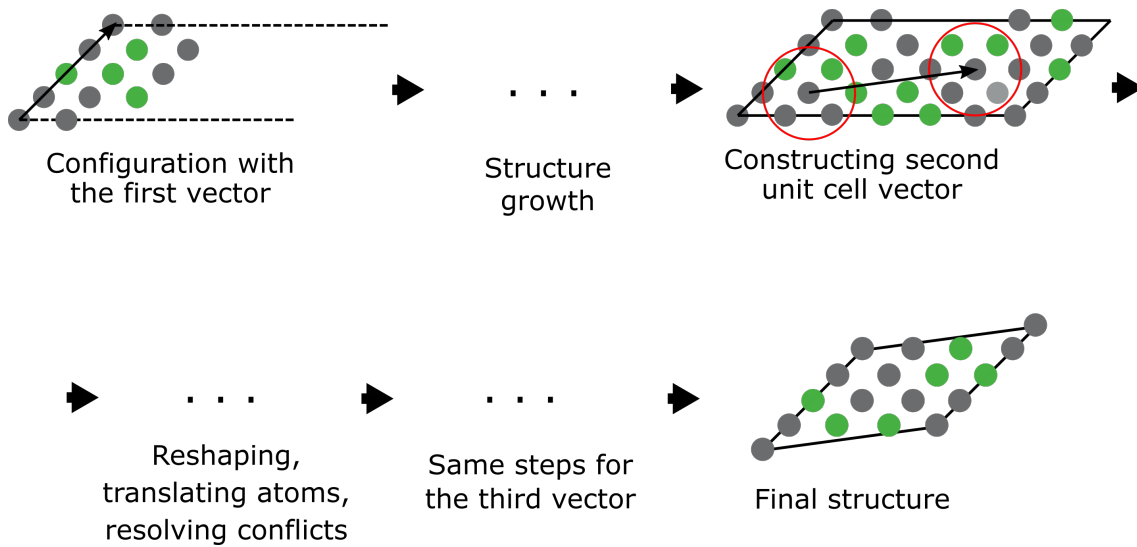


Figure 3-3: Construction of second and third unit cell vectors and final structure.

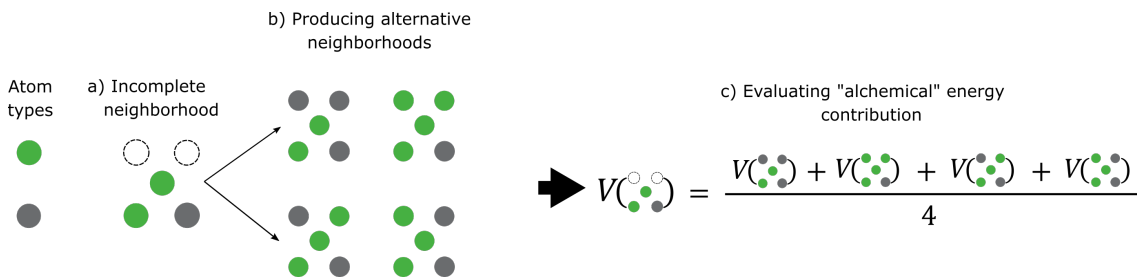


Figure 3-4: Schematic illustration of evaluation of energy contribution of an "alchemical" neighborhood.

3.2 On-lattice Canonical Monte Carlo method

Originally, Monte Carlo methods were developed for the study of stochastic processes. These methods investigate evolution of the system based on repeated random sampling from the unknown distribution. In materials science, Monte Carlo is used, for example, to study diffusion, simulate magnetic properties of materials, or detect a thermodynamically stable atomic structure. In this work canonical Monte Carlo method, adapted for the case of fixed atomic positions, is used.

Most of the Monte Carlo methods, including the one used in this work, are based on Markov process, where the current state of a system A depends on its previous state. Hence, the expectation value of a thermodynamic quantity F can be

represented as a sum over quantities, evaluated at all the previous steps, multiplied by their probability:

$$\bar{F} = \sum_{A_i} F(A_i)u_i, \quad (3.2)$$

where A_i is the state of a system, $F(A_i)$ is the function, raising a thermodynamic quantity of a system in the state A_i and u_i is a probability, determined by the Boltzmann distribution:

$$u_i = \frac{e^{E_i/kT}}{\sum_{A_j} e^{E_j/kT}}, \quad (3.3)$$

where E_i is the internal energy of the system in the state A_i . Since u_i measures the probability of a system being in the state A_i , it should satisfy the normalization requirement:

$$u_i \geq 0, \sum_i u_i = 1. \quad (3.4)$$

Using Markov chains it is possible to obtain a set of states A_1, \dots, A_M with a corresponding set of thermodynamic quantities $F(A_1), \dots, F(A_M)$. Hence, the expected value of a thermodynamic quantity, obtained over M steps will be:

$$\bar{F} = \frac{1}{M} \sum_{i=1}^M F(A_i) \quad (3.5)$$

Let us now consider how the system transits between these states in the calculations. The most computationally efficient approach of constructing the chain of states is called importance sampling. Let p_{ij} be the probability of a transition between the states A_i and A_j . Then, in order to transit from A_i to A_j we generate a random number ε , uniformly distributed between 0 and 1. If $p_{ij} \geq \varepsilon$ the system goes to the state A_j . Importance sampling allows to avoid evaluation of irrelevant regions of a phase space, still providing the exact solution to the problem.

In Monte Carlo simulations, performed in this work, the system is represented by an atomic configuration on a given crystalline lattice with a fixed concentration and number of atoms N . The candidate state A_j is prepared by the exchange of two atoms on neighboring lattice sites. The general algorithm of the method is the following:

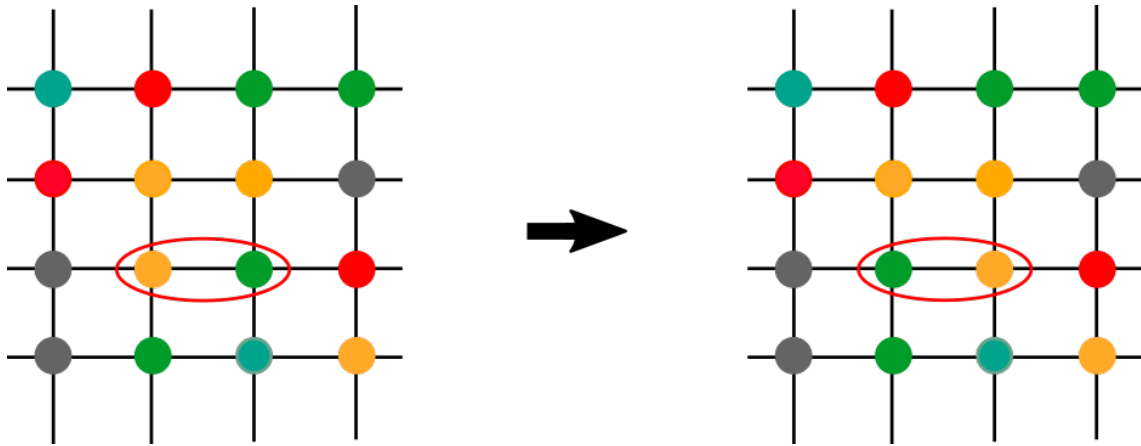


Figure 3-5: Illustration of a site exchange during canonical Monte Carlo simulation.

1. Random atomic configuration is generated
2. The random site of a crystalline lattice is selected (with probability $\frac{1}{N}$)
3. The neighboring site of the site, chosen during the step two, is selected
4. Atoms on this neighboring sites are exchanged as shown on Fig.3-5
5. The energy difference ΔE between configurations before and after the exchange is evaluated. The probability of this exchange is calculated using Eq. 3.3
6. A random number $\varepsilon \in (0, 1)$ is generated. If $u_i \geq \varepsilon$ the new configuration is accepted
7. The desired thermodynamic variables are evaluated.

This cycle is repeated until evaluated thermodynamic quantities converge. In this work the described Monte Carlo method is used with the LRP potential. This combination allowed to perform simulations at much larger scales than DFT, maintaining accuracy of the latter.

The combination of CMC with the LRP was used to study phase stability of a wide range of multicomponent alloys including NbMoTaW [Kostiuchenko et al. \[2020\]](#), VCoNi [Kostiuchenko et al. \[2019\]](#). Further, it was shown, that the method can go beyond metallic systems on the example of carbides [Pak et al. \[2023\]](#) and also can implicitly account for magnetic interactions in CrCoNi [Ghosh et al. \[2022\]](#).

3.3 Modeling procedure

The main bottleneck in most of the machine-learning based materials simulations is the large number of computationally expensive DFT calculations required for the training set. In this work a special strategy, called active learning, is applied. Active learning is an iterative process, which consists of a simulation, the following selection of the obtained configurations, and DFT calculations. With this approach the number of expensive DFT calculations can be reduced to an amount sufficient for a construction of a representative dataset. Active learning was used in both on-lattice CSP and on-lattice Monte Carlo simulations, albeit with minor differences.

3.3.1 Modeling with on-lattice CSP

To obtain an accurate potential for on-lattice CSP simulations a procedure shown on Fig. 3-6 was used. It starts with constructing the initial DFT convex hull. After, on-lattice CSP simulations are performed and the LRP/CE convex hull is constructed. Then, the structures obtained within 5 meV/atom interval above the LRP/CE convex hull are selected for DFT post-relaxation. Finally, post-relaxed structures are added to the DFT convex hull. The simulation terminates if the DFT convex hull stops updating. The process of constructing the LRP/CE convex hull should be explained in more details. On-lattice CSP simulation starts with the initial LRP/CE convex hull and iteratively updates each simplex. The schematic illustration of this process is presented on Fig. 3-7. As seen, the initial convex hull contains one simplex formed by unary structures. To update it, on-lattice CSP tries to generate a configuration with the energy below this simplex (Fig. 3-7a). After, in the similar manner, the algorithm tries to update the simplex 1 of the new convex hull (Fig. 3-7b-c) and so on. In such a way the algorithm iterates over each simplex. On average $10^4 - 10^6$ iterations are required to construct the final LRP/CE convex hull.

3.3.2 Modeling with on-lattice Monte Carlo

Thus, to obtain an accurate LRP for on-lattice Monte Carlo simulations a procedure shown on Fig.3-8 was used. As seen, the process starts with some initial dataset with a limited amount of DFT data. After, LRP/CE is trained using the initial training set. Further, the simulation is performed using the obtained LRP/CE. During the simulation additional configurations are sampled. In case of on-lattice Monte Carlo the structures are sampled from the temperature regions with observed anomalies, represented by an abrupt changes in specific heat capacity. As a rule, after several selection rounds the RMSE falls below 10 meV/atom.

To assess the effectiveness of the developed methods, I used them to study several multicomponent systems. At first, using on-lattice CSP with the LRP and CE I constructed convex hull of Nb-W, Mo-Ta-W and Nb-Mo-Ta-W systems. Next, using on-lattice Monte Carlo with LRP I investigated the phase stability of HfTaTiNbZrC₅ solid solution. For the first time it was shown that the proposed approach can be also applied to carbides. Finally, the same methodology was applied to study phase stability and SRO in CrCoNi medium-entropy alloy. The results will be presented in the corresponding order starting with investigation of phase stability in Nb-Mo-Ta-W chemical space.

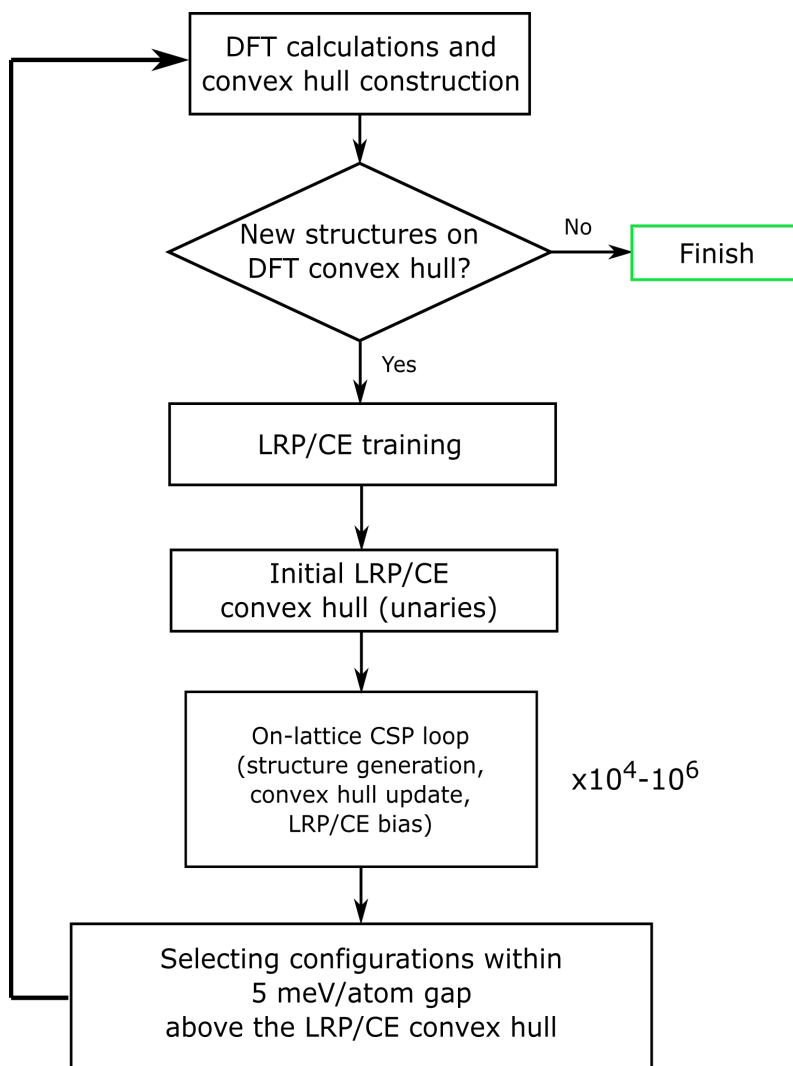


Figure 3-6: On-lattice CSP modeling procedure.

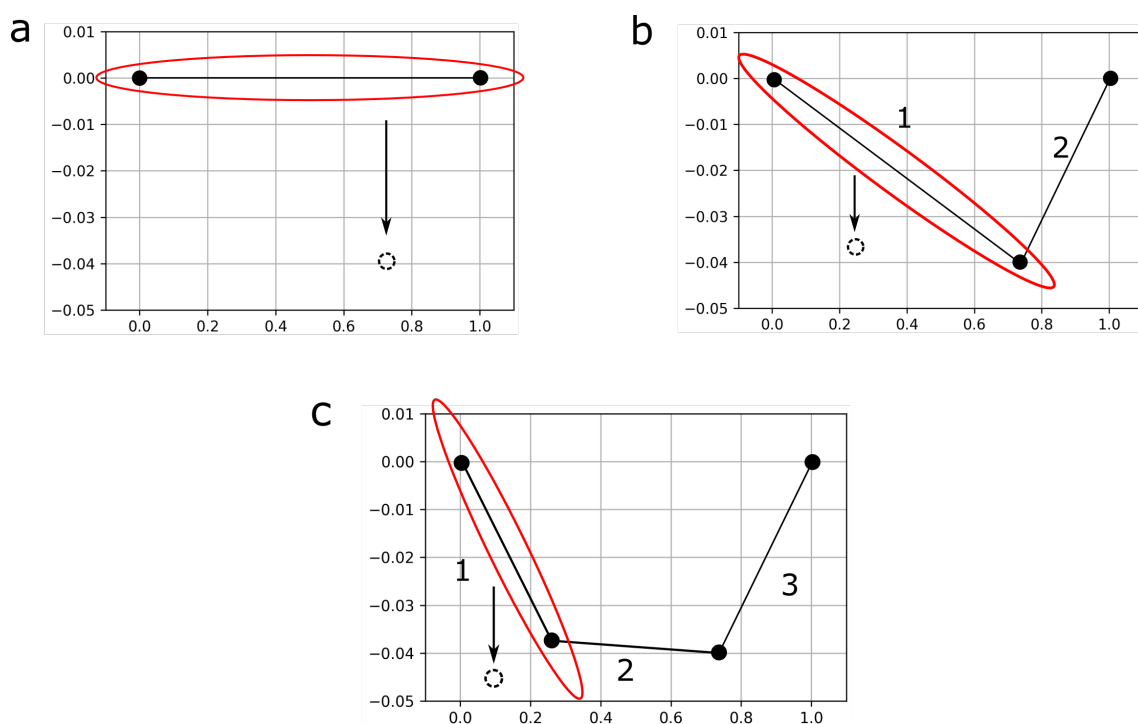


Figure 3-7: Convex hull construction with on-lattice CSP simulation. A potentially new point on convex hull is marked with a dashed circle.

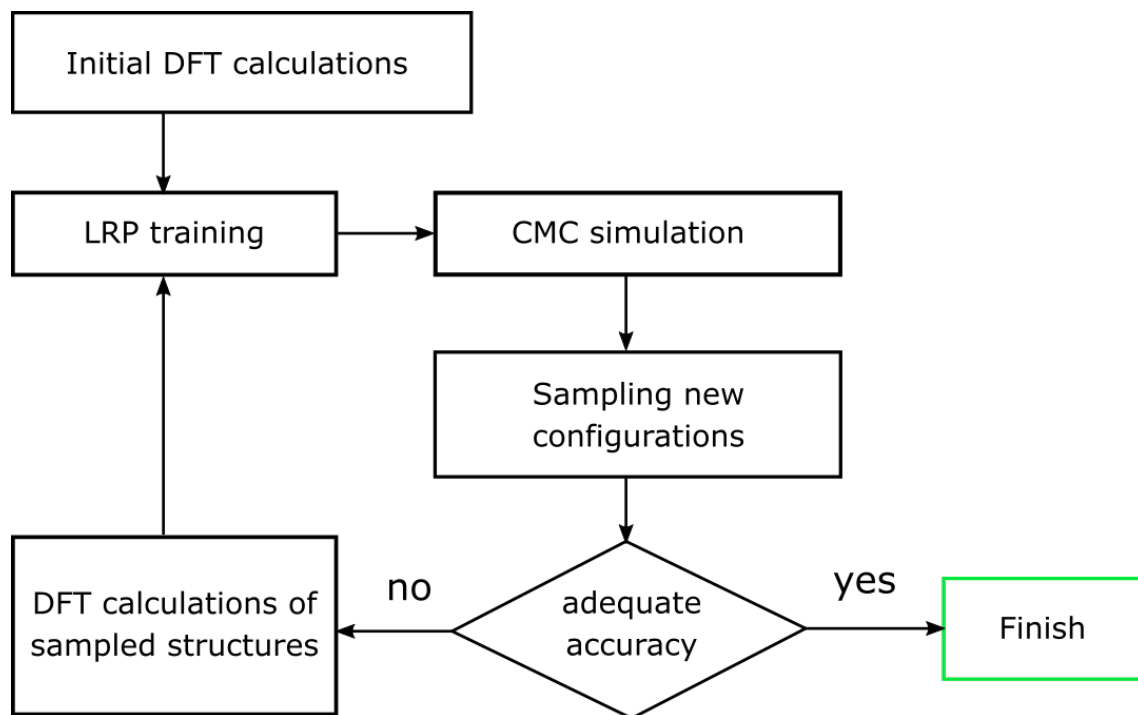


Figure 3-8: Algorithm for obtaining an accurate LRP during on-lattice CMC simulations.

Chapter 4

Investigation of Nb-Mo-Ta-W system with on-lattice CSP

The on-lattice CSP was applied to discover stable structures in Nb-Mo-Ta-W chemical system. While this system has a dozen of reported stable binary and ternary structures, little information is available about the stable quaternary compounds. Recently, an LRP driven on-lattice Monte Carlo simulation of equimolar NbMoTaW was performed by [Kostiuchenko et al. \[2019\]](#). The studies revealed that the ground state structure is a combination of B2(MoTa) and B32(NbW) phases with formation enthalpy of 118 meV/atom. With the impact of lattice relaxations during DFT calculations the reconsidered LRP provided a lower ground state with formation enthalpy of -124 meV/atom. The obtained structure was a combination of Nb-Mo-Ta-W-W-Mo-Nb layers. In another work by [Widom \[2016, 2018\]](#) a cluster expansion energy-based Monte Carlo revealed an even lower ground state with formation enthalpy of -126 meV/atom. The studies revealed that the obtained ground state decomposed into hR7(Mo₂NbTa₂W₂) and cI2(Nb). Such discrepancies in the mentioned studies suggest that there might be another low lying equimolar ground state. Moreover, investigations of other ground state compositions have not been performed to date. In this work I apply on-lattice CSP to discover new stable compositions. At first the method is validated on binary Nb-W and ternary Mo-Ta-W systems, and after it is applied to quaternary Nb-Mo-Ta-W.

4.1 Calculation details

The CE as well as LRP, which were used as interaction models in on-lattice-CSP, were trained on DFT calculations. To compute reference energies for the training, VASP 5.4.4 [Kresse and Furthmüller \[1996\]](#), [Kresse and Hafner \[1993, 1994\]](#) was used. The projector augmented wave (PAW) [Blöchl \[1994\]](#) method utilizing the Perdew-Burke-Ernzerhof generalized gradient approximation (PBE-GGA) [Perdew et al. \[1996\]](#) was employed. The training set was constructed using an active learning approach. Reference configurations were obtained from on-lattice-CSP simulation and, hence, had variable number of atoms. For computational efficiency we selected configurations with no more than 16 atoms in the unit cell. The value of plane-wave cutoff energy was set to 400 eV, which is 1.8 times larger than the highest ENMAX energy of the utilized PAW pseudopotentials. To provide a stable convergence of calculations for different cell shapes and sizes, we employed an automatic generation of k-points grid using by setting KSPACING to 0.13. To account for the impact of lattice relaxations, both ionic and cell relaxations were included. The energy convergence criteria for these types of relaxations was set to 10^{-5} eV.

For each chemical system the initial lattice parameter was chosen as a mean of lattice parameters of unary structures. For example, taking $a_{\text{Nb}} = 3.30$ Å and $a_{\text{W}} = 3.16$ Å, the initial lattice parameter for Nb-W alloys is $a_{\text{Nb-W}} = 3.23$ Å.

For binary as well as ternary systems on-lattice CSP was used in combination with CE, since in this case it has accuracies comparable to that of LRP. In case of Nb-Mo-Ta-W the LRP was applied in order to limit the number of DFT calculations.

4.2 Nb-W

At first the method is applied to construct Nb-W convex hull. According to AFLOW database [Curtarolo et al. \[2012\]](#), this system has three stable binary phases, namely, NbW (B32), NbW₃ and NbW₇. Both pure Nb and W, as well as the stable binaries have bcc lattice, so this system is a good test of whether the method is able to discover the stable structures and reproduce the AFLOW convex hull.

The initial training set consisted of 3 configurations—unary Nb and W with one

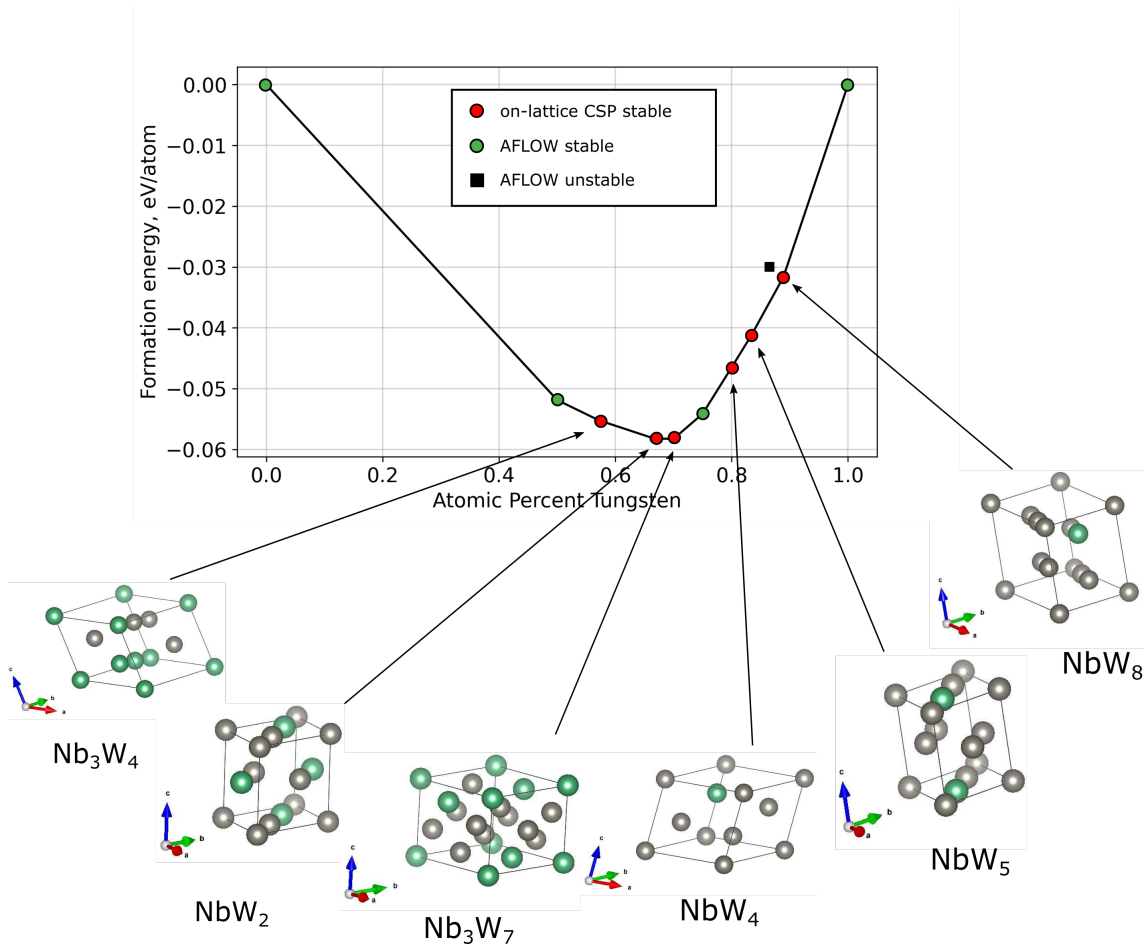


Figure 4-1: Final DFT Nb-W convex hull and unit cells of the new structures. Six new structures were discovered with on-lattice CSP (marked with red circles on the convex hull).

atom in the unit cell and the binary B2(Nb;W) structure. According to AFLOW phase diagram of Nb-W system B32(Nb;W) phase is the phase that is on the convex hull, while B2(Nb;W) has higher energy. Thus, for a fair benchmarking B32(Nb;W) was not added to the initial training set. During the simulation additional 114 configuration were sampled from LRP/CE convex hull. Thus, the final training set consisted of 117 configuration raising a RMSE of 5.31 meV/atom.

Fig. 4-1 shows the convex hull, constructed by CSP-on-lattice and post relaxed with DFT. As it is seen CSP-on-lattice was able to predict all the stable phases, reported in AFLOW (green and black markers), as well as 6 new structures (red markers). Among the new discovered compositions are Nb₃W₄, NbW₂, Nb₃W₇, NbW₄, NbW₅ and NbW₈. Their distance from AFLOW convex hull, measured in

Composition	Position below convex hull, meV/atom
Nb ₃ W ₄	-2.7
NbW ₂	-4.8
Nb ₃ W ₇	-4.6
NbW ₄	-1.3
NbW ₅	-2.0
NbW ₈	-3.4

Table 4.1: Position below convex hull of predicted Nb-W alloys.

meV/atom, is reported in Table 4.1. As it is seen, the new stable compositions were found within a W-rich area of a phase diagram. However, ground states with the largest distance from AFLOW convex hull, such as Nb₃W₄, NbW₂, Nb₃W₇, are observed closer to the center of a phase diagram, which indicates a significant contribution of Nb additions to a phase stability. Additionally, the NbW₇ phase, reported as a ground state in AFLOW database, became unstable having the energy above our convex hull of 2.3 meV/atom.

4.3 Mo-Ta-W

The on-lattice CSP next is tested on constructing the convex hull for the ternary Mo-Ta-W system. At first, the convex hull for the three binary subsystems, namely Mo-Ta, Mo-W and W-Ta was constructed and after the simulations were performed for Mo-Ta-W. The initial training set for Mo-Ta-W contained 4 configurations - unary Mo, Ta and W with 1 atom in the unit cell and a random MoTaW with 3 atoms in the unit cell. During the simulations 109 additional configurations were selected, including both binary and ternary structures in nearly equal proportion. The RMSE on the final training set was 8.34 meV/atom.

The resulting convex hull, post relaxed with DFT, is presented on Fig. 4-2. It has all the ternary phases present in AFLOW as well as two new - Mo₃Ta₃W, MoTa₂W₂. Additionally, three new binaries were discovered: TaMo₅, TaMo₆ and TaW₈. Since DFT was performed with automatic k-mesh generation, I accounted for a noise in our calculations and, thereby, also add the structures obtained within 1 meV/atom above the convex hull. Among such structures presented on Fig. 4-

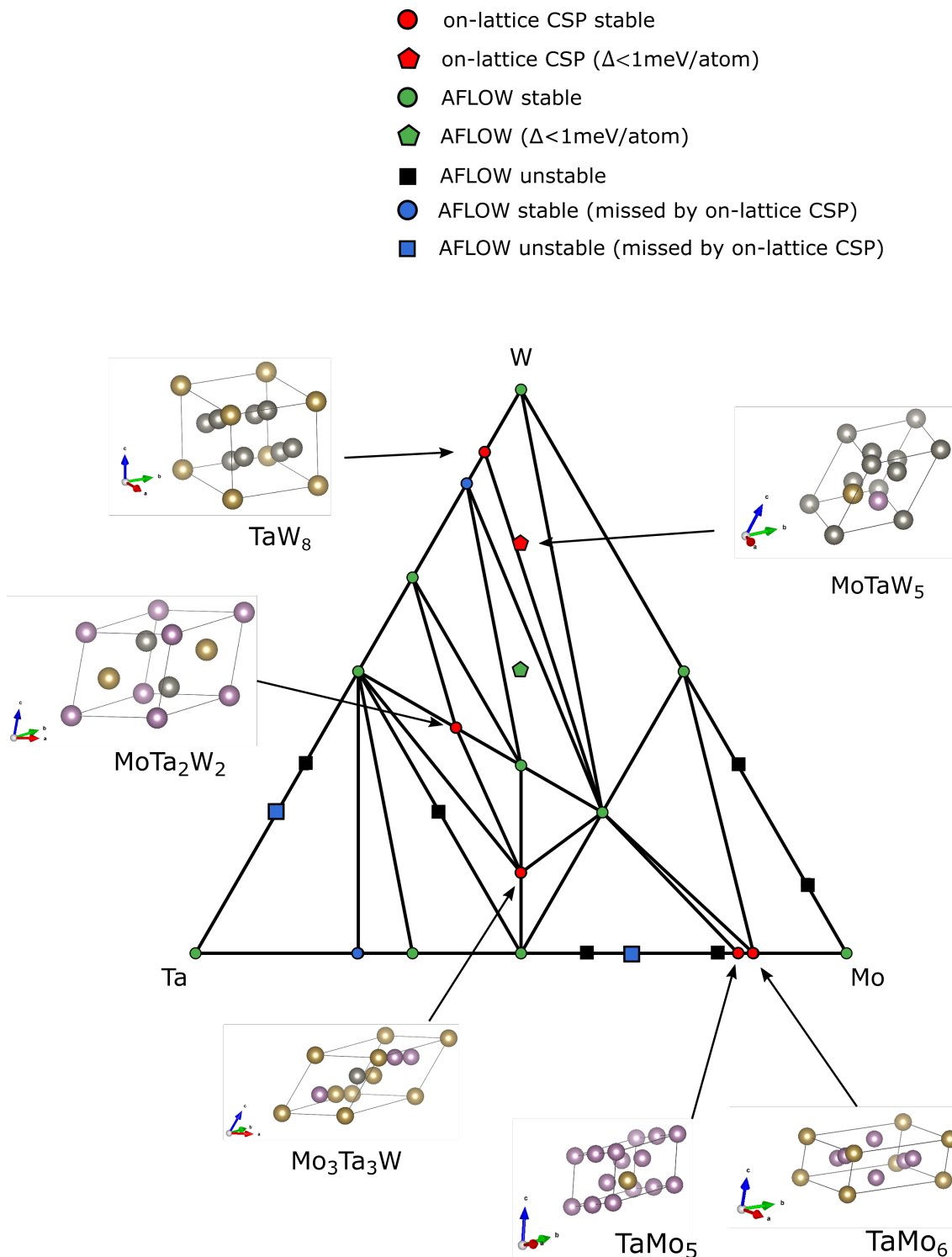


Figure 4-2: Final DFT Mo-Ta-W convex hull and unit cells of the new structures. Six new structures were discovered with on-lattice CSP (marked with red on the convex hull).

2, MoTaW₅ was newly discovered by on-lattice CSP, while MoTaW₂ is an AFLOW ground state structure. Among the new phases, Mo₃Ta₃W have the lowest formation

Composition	Formation enthalpy, meV/atom
MoTa	-187
Mo ₃ Ta ₃ W	-178
MoTaW	-145
MoTaW ₂	-114
MoTaW ₅	-69

Table 4.2: Formation enthalpies of MoTa-based alloys.

enthalpy of -178 meV/atom. Remarkably, MoTa-rich region of a phase diagram has another low-lying ground state, namely, equimolar MoTa with formation enthalpy of -187 meV/atom. Such findings reveal that MoTa-rich phases might possess a better phase stability, than structures from other regions of a phase diagram. This trend can be observed from the Table 4.2, where formation enthalpies for the phases with fixed concentration of Mo and Ta are presented. As it is seen, formation enthalpy increases from -187 meV/atom when no W is present in an alloy, to -69 meV/atom when concentration of W exceeds 70 %.

4.4 Nb-Mo-Ta-W

Finally, the method was applied to construct the quaternary Nb-Mo-Ta-W convex hull. For the evaluation of energy of quaternary systems I used LRP as it requires less DFT data for obtaining an adequate approximation accuracy as compared to CE. The initial training set was constructed in a similar manner. That is, it had five configurations—unary Nb, Mo, Ta and W as well as a random quaternary NbMoTaW. After the simulation the training set was extended to 380 configurations among which 114 structures had quaternary composition. The RMSE on this training set was 7.1 meV/atom.

The resulting convex hull, post relaxed with DFT, is presented on Fig. 4-3. It contains all the structures previously discovered by on-lattice CSP as well as all the stable phases reported in AFLOW, where some of them were missed by the algorithm (marked as blue). Also, I added a quaternary NbMo₂Ta₂W₂ ground state phase, reported by M. Widom [Widom \[2016\]](#), which has the formation enthalpy of -145

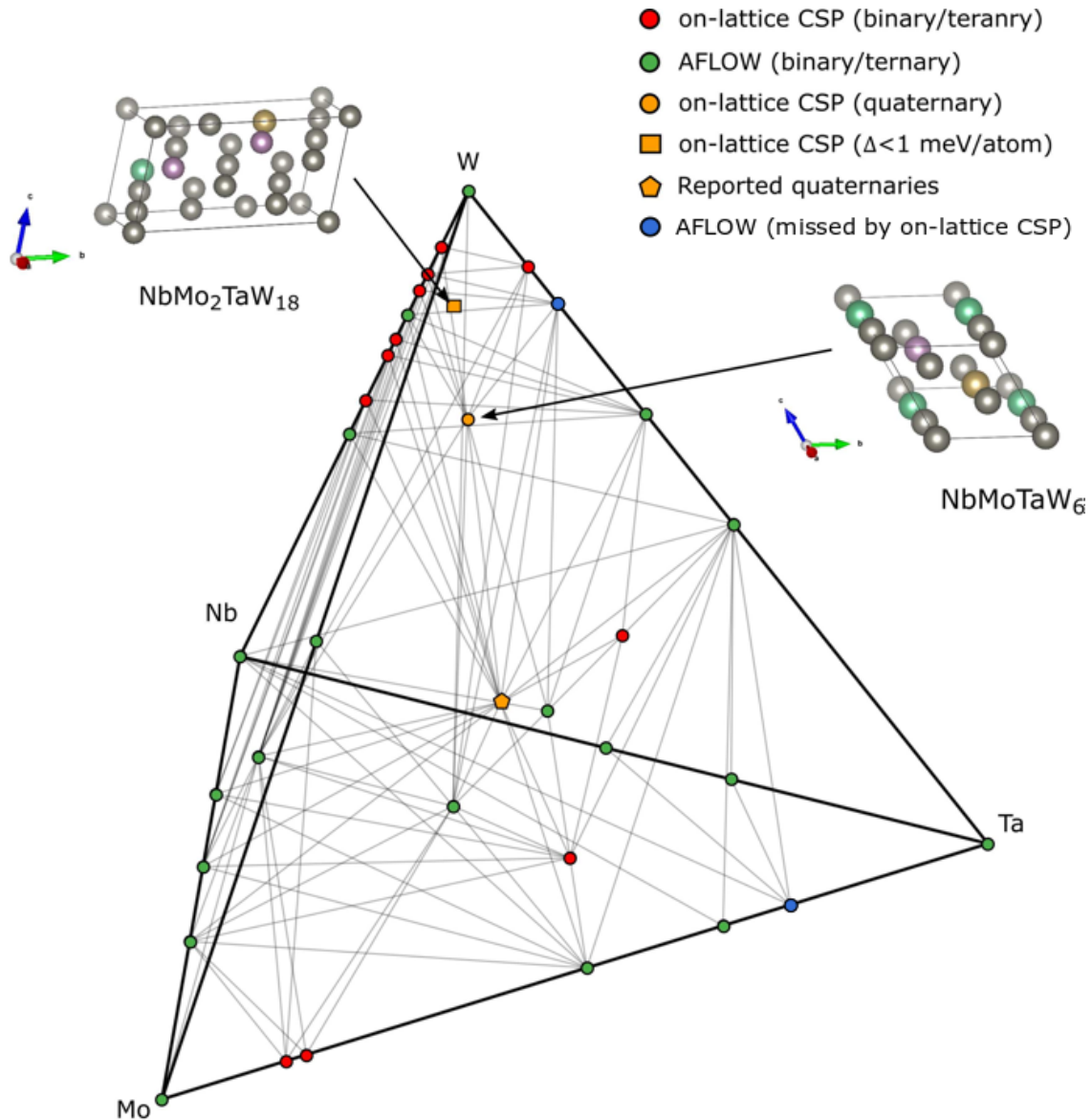


Figure 4-3: Final DFT Nb-Mo-Ta-W convex hull and unit cells of the new structures. Two new quaternary structures (9-atom NbMoTaW_6 and 22-atom $\text{NbMo}_2\text{TaW}_{18}$) were discovered. Stable structures discovered with on-lattice CSP are marked with orange circles and squares on the convex hull.

meV/atom. As it is seen the algorithm has discovered one new quaternary ground state composition— NbMoTaW_6 with the formation enthalpy of -78 meV/atom. Interestingly, NbMoTaW_6 as well as the majority of other discovered structures are W-rich phases, which makes their discovery relevant to the application of W-based alloys.

Carefully studying the structures, generated by the algorithm, I observed some amount of configurations with relatively large unit cells (>20 atoms). However, all

of them were lying higher than 5 meV/atom above LRP convex hull. To investigate their stability, the selection gap was increased to 10 meV/atom and the structures were selected for post-relaxation. Among them, I discovered a 22-atom near-stable NbMoTa₂W₁₈ with distance above convex hull of 0.9 meV/atom. Such findings indicate, that the algorithm is also capable of discovering stable structures with large unit cells without employing extensive computational resources.

Note that in this work all the predicted phases are benchmarked with AFLOW database, that contains only 0 K DFT calculations. Thus, phase stability of the predicted phases at finite temperature is not investigated. However, it is assumed that all the discovered phases remain ordered within a moderate range of temperatures (0 - 300 K), i.e. they are not approximations of high-temperature disordered phases. Investigation of order-disorder phase transition in Nb-Mo-Ta-W alloys is out of the scope of this work.

In general, the advantage of on-lattice CSP in comparison with the state-of-art CSP methods like USPEX can be observed when discovering materials with a pre-defined lattice. For example, USPEX was used to search the structures in quaternary C-H-N-O chemical space, where configurations have an undefined geometry Naumova et al. [2021]. USPEX runs were performed with 8-36 atoms per unit-cells. Eventually nearly 1800000 DFT structural relaxations were performed, which require significant computational resources. In case of Nb-Mo-Ta-W alloys, that are presented in this work, only a few hundreds of DFT calculations were required. Such reduction, first of all, is possible due to application of LRP and CE for energy evaluation. Secondly, the presence of a fixed geometry significantly reduces the size of the configurational space of candidate materials. Moreover, the presented algorithm can discover multicomponent structures among supercells with larger number of atoms. Thus, several structures, discovered in Nb-Mo-Ta-W, had more than 140 atoms in the supercell. Though on-lattice CSP can't operate in cases of an undefined geometry (which is a significant drawback in comparison with USPEX), the main takeaway of this work consists in possibility of applying a conceptually new generative approach in the CSP field. The extension of on-lattice CSP to materials with the undefined lattice geometry can be done by combining the algorithm with

geometry-sensitive potentials like MTP. Once an atom is added to the structure, the growing configuration can be relaxed with the MTP. Thus, the geometry is defined in real time. Such direction is of high scientific importance and is expected to be performed in the future.

Chapter 5

Investigation of phase stability of HfTaTiNbZrC₅ high-entropy carbide

High-entropy carbides have been a subject of intensive both experimental and theoretical investigation recently [Castle et al. \[2018\]](#), [Oses et al. \[2020\]](#), [Hossain et al. \[2021\]](#). These materials attracted significant attention due to their enhanced refractory properties and corrosion resistance. They form a rock-salt fcc lattice, where carbon atoms occupy $4b$ and metallic atoms - $4a$ Wyckoff positions. The most common method to synthesize high-entropy carbides is reactive spark plasma sintering (SPS) of pre-homogenized raw materials based on individual metal carbides, pure metals or metal oxides [Demirskyi et al. \[2020\]](#), [Li et al. \[2021\]](#). However, the successful synthesis of a solid solution cannot be performed every time, since the temperature conditions responsible for the formation of that phase have not been studied yet. As a consequence, a temperature window of a stable solid solution remains unknown.

In the present work, on the example of HfTaTiNbZrC₅, Monte Carlo simulation combined with the LRP is performed to determine solid solution formation temperature and investigate its phase-stability. Also, it is shown that the obtained theoretical results can be used to provide a controllable synthesis of HfTaTiNbZrC₅ solid solution phase.

5.1 Calculation details

To obtain the LRP with an adequate accuracy, the algorithm described in Chapter 2 was employed. The initial dataset contained 150 random configurations with an fcc lattice, where metallic and carbon atoms occupy positions (0, 0, 0) and (0.5, 0.5, 0.5), respectively. The size of each configuration was $2 \times 2 \times 2$ (32 atoms), confined to be as equimolar as possible. During subsequent Monte Carlo simulations additional configurations were sampled for LRP retraining. After performing several iterations of this scheme, 250 new configurations were added to the initial dataset. The final dataset was split into training and validation subsets with 350 and 150 configurations respectively. The RMSE on the validation set was 9 meV/atom.

The total energies of the sampled configurations were calculated using DFT. Their computation was performed by VASP 5.4.4 [Kresse and Furthmüller \[1996\]](#), [Kresse and Hafner \[1993, 1994\]](#) with the projector augmented wave (PAW) [Blöchl \[1994\]](#) method utilizing the Perdew-Burke-Ernzerhof generalized gradient approximation (PBE-GGA) [Perdew et al. \[1996\]](#). The value of plane-wave cutoff energy was set to 540 eV. For Brillouin zone sampling a $4 \times 4 \times 4$ k -point mesh was generated using the Monkhorst-Pack scheme [Monkhorst and Pack \[1976\]](#). To account for the impact of lattice relaxations, both ionic and cell relaxations were included.

To perform miscibility analysis of competitive binary and ternary phases the vibrational contribution to the free energy was also included. The stability of the competitive phases was analyzed by calculating Helmholtz free energy at finite temperature (the pressure was neglected since the experiment was conducted under atmospheric pressure) using the following expression:

$$F_{\text{mix}}(T) = \frac{F_{\text{tot}}(T) - \sum_i N_i F_i^{\text{MeC}}(T)}{\sum_i N_i}, \quad (5.1)$$

where F_{tot} is the Helmholtz free energy of competitive carbide, F_i^{MeC} is the Helmholtz free energy of a constituent individual carbide and N_i is its molar fraction in the competitive compound. The values of F_{tot} and F_i^{MeC} can be calculated using the

following expression:

$$F(T, V) = E_0(V) + F_{\text{vib}}(T, V) - TS_{\text{conf}}, \quad (5.2)$$

where E_0 is the total energy from the DFT calculations, TS_{conf} is the configurational entropy, F_{vib} is the vibrational correction calculated from the phonon density of states by using following relation in the harmonic approximation Kern et al. [1999]:

$$\begin{aligned} F_{\text{vib}}(T, V) = & k_{\text{B}}T \int_{\Omega} g(\omega(V)) \times \\ & \times \ln \left(1 - e^{-\frac{\hbar\omega(V)}{k_{\text{B}}T}} \right) dx + \\ & + \frac{1}{2} \int g(\omega(V)) \hbar\omega d\omega, \end{aligned} \quad (5.3)$$

Here $g(\omega(V))$ is the phonon density of states at a given volume, calculated using the finite displacements method as implemented in PHONOPY Togo et al. [2008] with forces computed using VASP Kresse and Furthmüller [1996], Kresse and Hafner [1993, 1994].

To evaluate temperature-dependent specific heat capacity configurational energies were collected over N steps of CMC at each temperature. Specific heat capacity then is calculated as follows:

$$C_{\text{V}}(T) = \frac{\sigma^2}{n(kT)^2}, \quad (5.4)$$

where σ^2 - energy variance, calculated over a number of CMC steps; n - number of atoms; k - Boltzmann constant; T - heating temperature.

5.2 Results of HfTaTiNbZrC_5 study

Before starting the simulation I investigated the probability of carbon atoms to diffuse between $4b$ and $4a$ sites. Eventually, it was observed that the energy of the supercells where carbon atoms occupy uncharacteristic $4a$ sites were higher by 6 eV on average than in the case when carbon resides strictly on $4b$ sites. Such

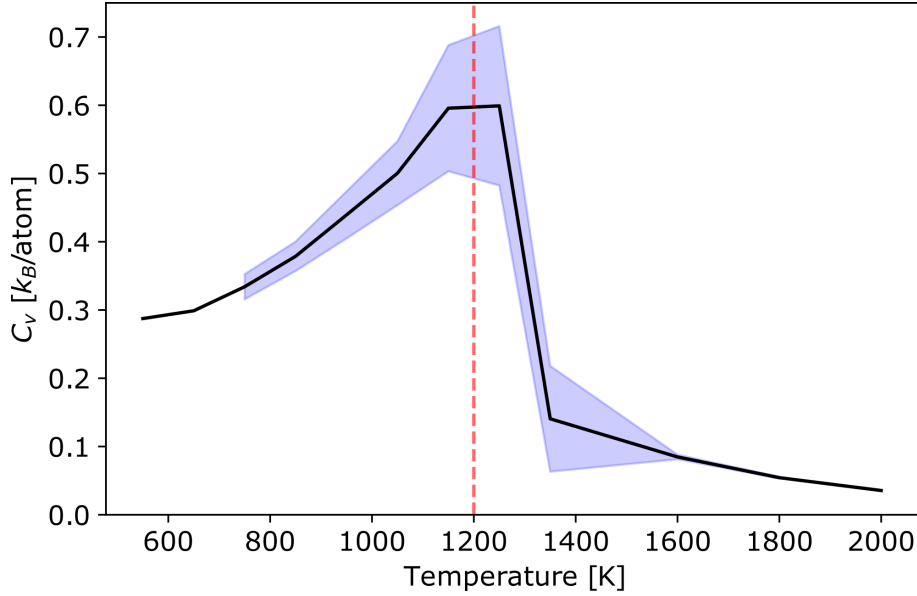


Figure 5-1: Specific heat capacity $C_V(T)$ for *fcc* TiZrNbHfTaC_5 from CMC simulations for a $10 \times 12 \times 15$ simulation box. Vertical dashed line marks the probable phase transition. Blue shaded area indicates a standard deviation calculated from 40 independent runs for each temperature.

results reveal that carbon-metal interchange is a less favorable event and, hence, it was not considered in the CMC simulations. However, carbon-metal interactions were implicitly taken into account by training the LRP on DFT calculations with included carbon atoms.

For a thorough study of a phase stability in multicomponent alloys it is vital to perform a large-scale simulations (i.e., in large simulation cells). The reason for that is an entropy contribution, which might be significant even at ambient temperatures. As a result, these alloys might not have any observable long-range order, and hence the true experimental phase cannot be approximated by the small simulation cells. Thus, in this work the CMC simulations were performed on $10 \times 12 \times 15$ supercell (7200 metallic atoms).

To investigate temperature dependent phase transition, specific heat capacity of TiZrNbHfTaC_5 was calculated between 500 K and 2000 K with a 100 K step. After evaluating c_v at each round of CMC run, the temperature dependent behavior of heat capacity was analyzed. At each round of the simulation the resulting curve had a temperature region with an abrupt peak in c_v value, which might reflect a potential

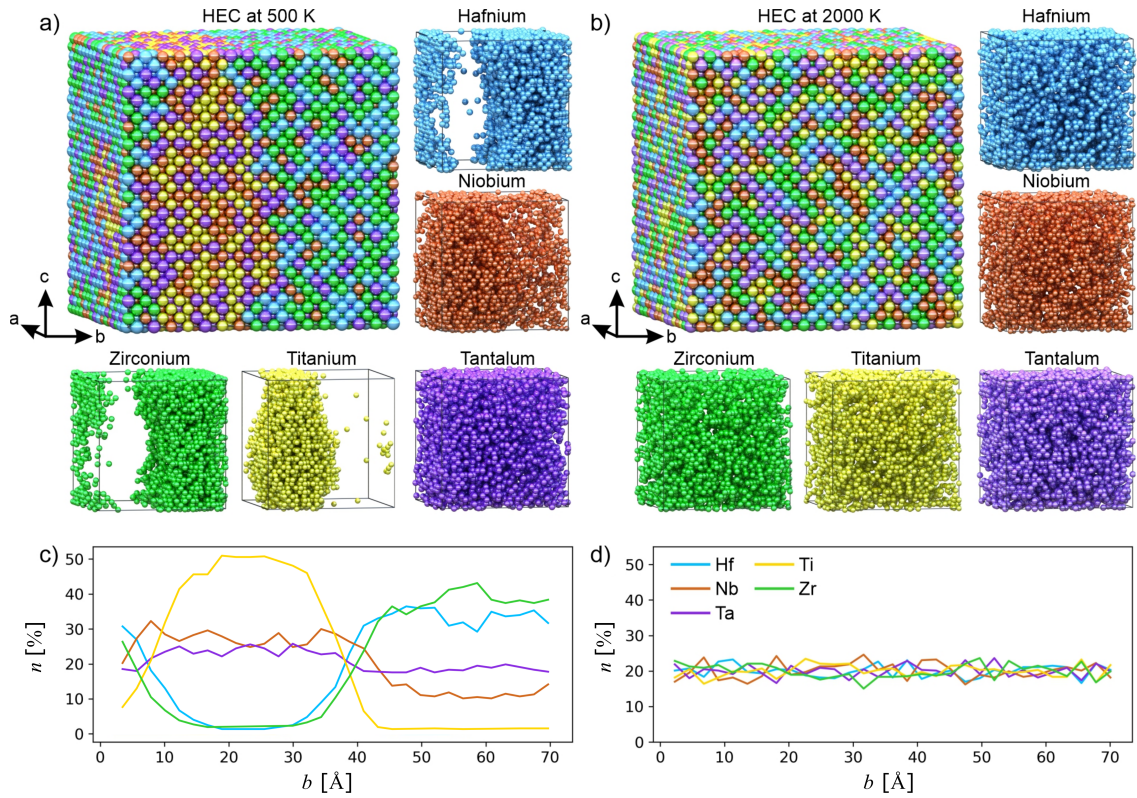


Figure 5-2: Crystal structures of the simulated $16 \times 16 \times 16$ supercell of a) multi- and b) single-phase $(\text{Ti-Zr-Nb-Hf-Ta})\text{C}$ at 500 and 2000 K respectively. Carbon atoms are not shown here explicitly to make the distribution of metal atoms clearer, while carbon atoms were considered in the MC simulations; c,d) relative concentration of chemical elements per layer along the supercell vector b .

phase transition in this area. To refine the results, additional configurations were sampled from this region for the LRP retraining. The final dependence of specific heat capacity on temperature is presented on Fig. 5-1. The black curve corresponds to a mean value of c_v , calculated over 40 independent CMC runs. As it is seen, the peak of c_v is observed in the region of 1100-1300 K. To estimate the phase transition temperature more precisely, the standard deviation between 40 independent CMC runs was evaluated (marked as a blue shaded area). The highest uncertainty is observed near 1200 K, which indicates that phase transition in TiZrNbHfTaC_5 is likely to occur at $T_c = 1200$ K.

Next I analyzed the resulting structures below and above the phase transition temperature. The corresponding supercells are presented on Fig. 5-2. An ideal solid solution was observed above T_c , namely at 2000 K. The corresponding supercell is

shown on Fig. 5-2b. As seen in the figure, metallic elements have are uniformly distributed along the simulation cell. This is additionally underlined in Fig. 5-2c, where concentration of metallic elements in each layer along the supercell vector b is depicted. The formation of solid solution at $T = 2000$ K is a clear consequence of an increased contribution of $-T\Delta S_{\text{mix}}$ term.

To further validate the results, an experimental synthesis of TiZrNbHfTaC_5 sample was performed. The synthesis was done using arc plasma sintering method, parameters of which were adjusted according to the results of CMC simulation. Thus, in order to provide a sintering temperature close to 2000 K, the direct current of an arc plasma spark was set to 200 A, which provided temperature of 2150 °C. The SEM images of an experimental sample with energy dispersive X-ray analysis is presented on Fig. 5-3a. Each color corresponds to a certain chemical element of the sample. Visually, the intensity of the diffracted X-ray irradiation has a uniform distribution along the sample for every chemical element, which confirms that the sample obtained at temperatures near 2000 K corresponds to an ideal solid solution. To provide a quantitative analysis experimental and theoretical X-ray diffraction diagrams of a solid solution (single) phase were constructed (Fig. 5-4a,c). As seen in the figure the XRD intensity peaks for both experimental and simulated samples are observed at the same values of diffraction angle. The XRD diagram of an experimental sample also contains peaks, corresponding to oxide clusters, but their concentration is negligible. Finally, a comparison between lattice parameters of experimental and theoretical phases was performed. To calculate the lattice parameter of the simulated phase a 32-atom supercell was extracted from the simulation domain and post-relaxed with DFT. Eventually, a good agreement between theoretical and experimental values was observed, having $a_{\text{sim}} = 4.51 \text{ \AA}$ and $a_{\text{exp}} = 4.49 \pm 0.03$.

A more interesting picture was observed at temperatures below T_c . At $T = 500$ K the sample decomposed into separate multi-component phases. As seen in Fig. 5-2a, TaC is uniformly distributed along the supercell, while HfC and ZrC do not tend to mix with TiC and NbC. According to the concentration distribution (Fig. 5-2c), concentration of TaC changes moderately across the supercell and average deviation does not exceed 8%. On the contrary, TiC concentration increases in the region

above 30 Å and saturates at 50 Å, while concentrations of HfC and ZrC decrease towards zero within the same area. Thus, one of the phases that emerges is (Ti-Nb-Ta)C. Additionally, as seen in Fig. 5-2a,c, NbC expresses a moderate tendency to mix with ZrC and HfC, preferring to form a solid solution with TiC phase instead. Since NbC still has the lowest concentration in ZrC/HfC-rich area the second phase can be either a mixture of (Zr-Hf-Ta)C and (Zr-Nb-Hf)C or four-component (Zr-Hf-Ta-Nb)C phases with binary (Zr-Nb)C and (Zr-Ta)C. The calculated lattice parameters of these phases are $a_1 = 4.45$ Å for (Ti-Nb-Ta)C and $a_2 = 4.52$ Å for the second potential phase. A larger simulation structure of 32000 atoms is presented on Fig. 5-5.

An SEM image (Fig. 5-3b) with energy dispersive X-ray analysis of an experimental multi-phase sample also shows phase separation. To provide a more detailed information about the observed phases, experimental and theoretical XRD diagrams of multi-phase samples were constructed as shown in Fig. 5-4b. A good agreement between diffraction angles for experimental and simulated phases is again observed. For the theoretical XRD all the potentially emerged phases in Ti-absent region were taken into account. As seen in Fig. 5-4b,d XRD peaks for (Zr-Hf-Ta)C, (Zr-Nb-Hf)C, (Zr-Hf-Ta-Nb)C, (Zr-Nb)C and (Zr-Ta)C appear at almost the same diffraction angle, which supports the suggestion that one of these phases or their mixture can precipitate below T_c . To provide more insight, Helmholtz free energy of mixing for different competing phases at 500 K was calculated (see Calculation details). The trend between Helmholtz free energies of different carbide phases and lattice parameters are presented on Fig. 5-6. Carefully studying the trend it was observed that the two phases, corresponding to theoretical lattice parameters, are (Ti-Nb-Ta)C and (Zr-Hf-Ta)C. Moreover, these values are in a good agreement with the lattice parameters of the two experimentally observed phases ($a_1 = 4.45 \pm 0.01$ Å for the first solid solution and $a_2 = 4.59 \pm 0.02$ for the second) Hence, the second phase is more likely to be a random solution of Zr, Hf and Ta carbides.

One possible reason for the formation of these phases could be a difference between diffusion rates of constituent metallic atoms. This suggestion is supported by Castle et al. [2018], where the phase separation in (Hf-Ta-Zr-Nb)C and (Hf-Ta-Zr-

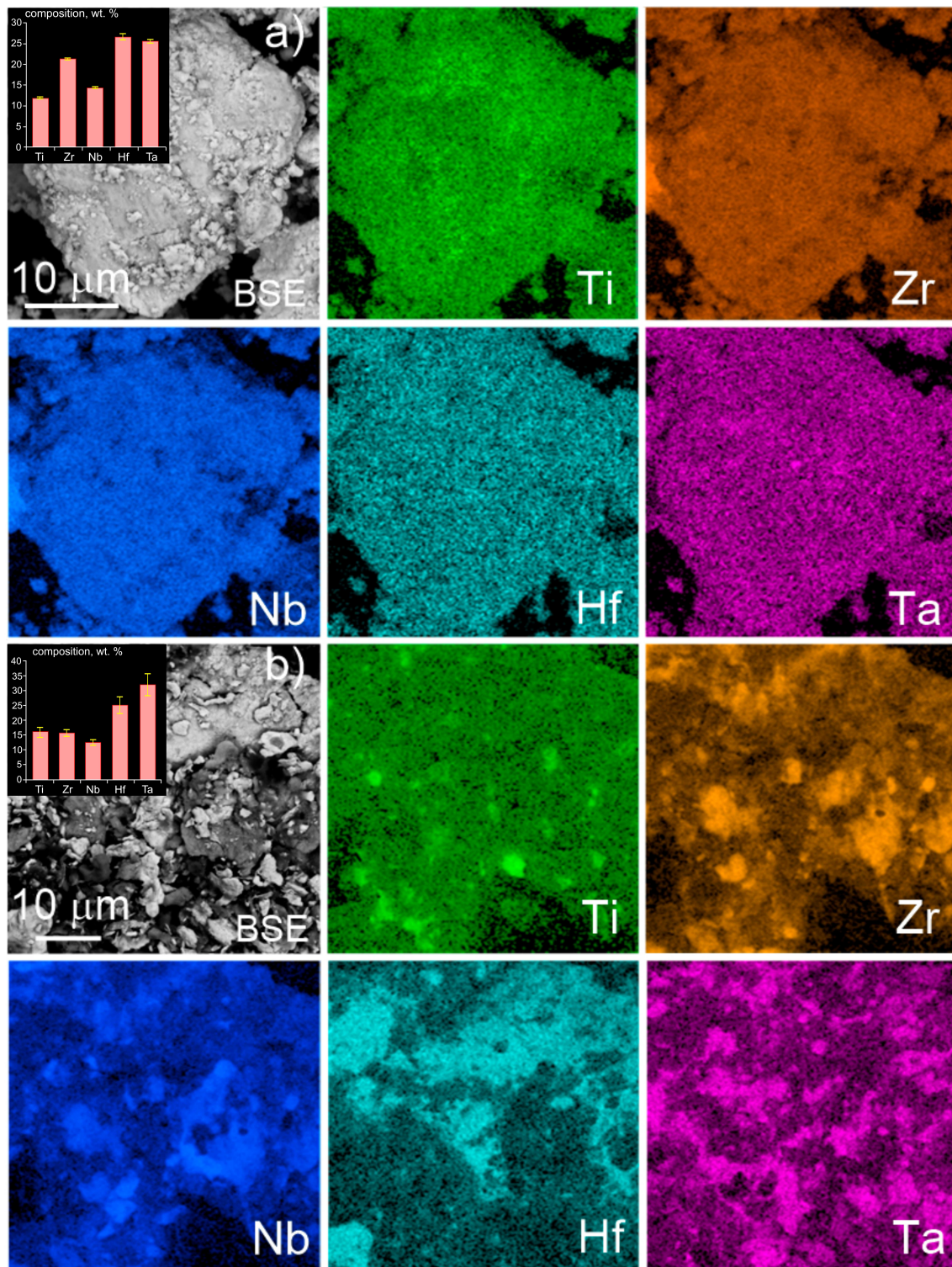


Figure 5-3: SEM images of experimental samples with energy dispersive X-ray analysis. a) Single- and b) multi-phase samples. Dispersive X-ray analysis images show the mapping of chemical elements across the sample. 20 points across the sample were used to measure the elemental distributions (shown in the inset).

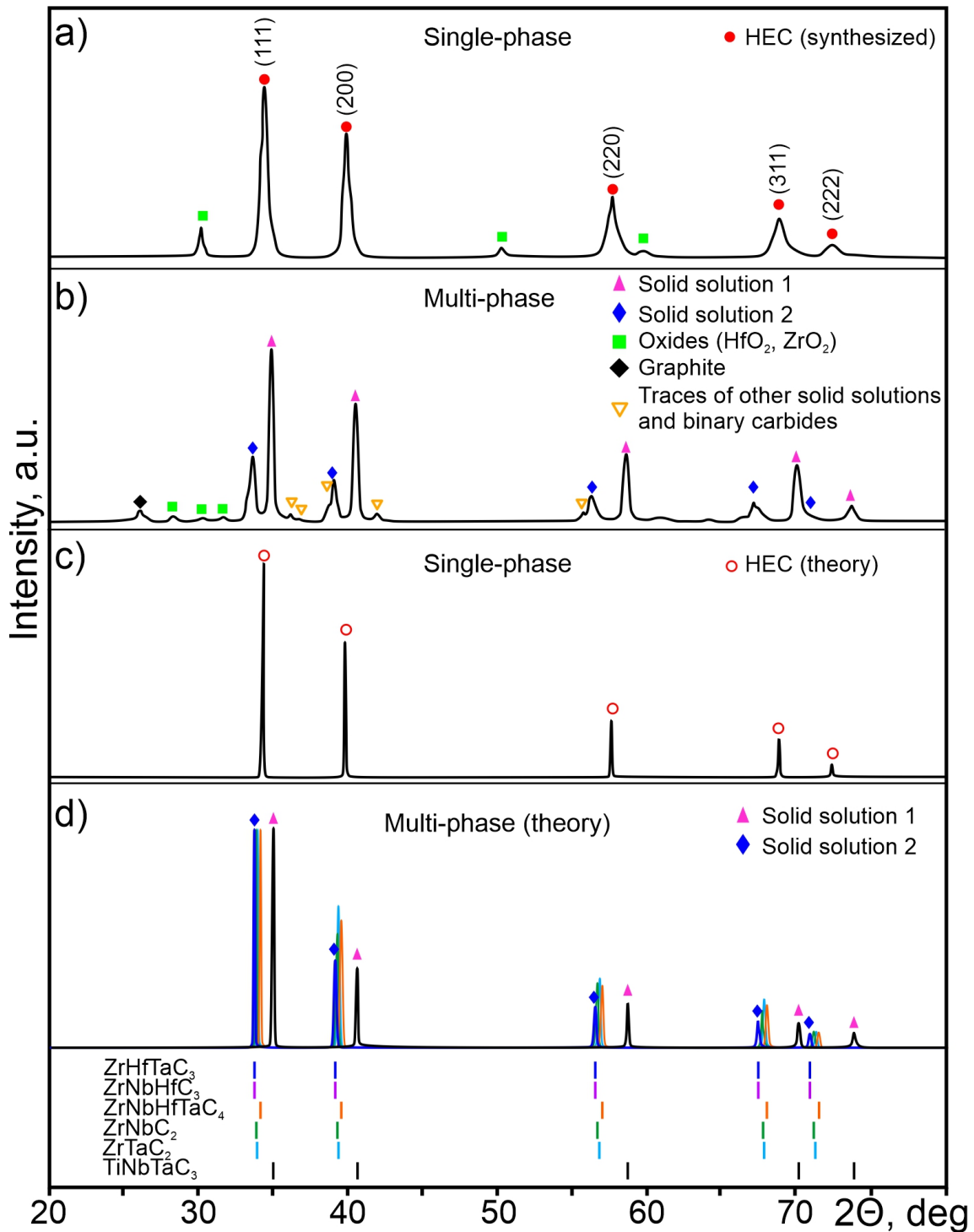


Figure 5-4: X-ray diffraction patterns of the synthesized a) single- and b) multi-phase samples of TiZrNbHfTaC_5 , and calculated XRD patterns of c) simulated single-phase HEC, and d) separate phases of ZrHfTaC_3 , ZrNbHfC_3 , ZrNbHfTaC_4 , ZrNbC_2 , ZrTaC_2 , and TiNbTaC_3 found by the analysis of calculated Helmholtz free energies of mixing of various multi-component carbides.

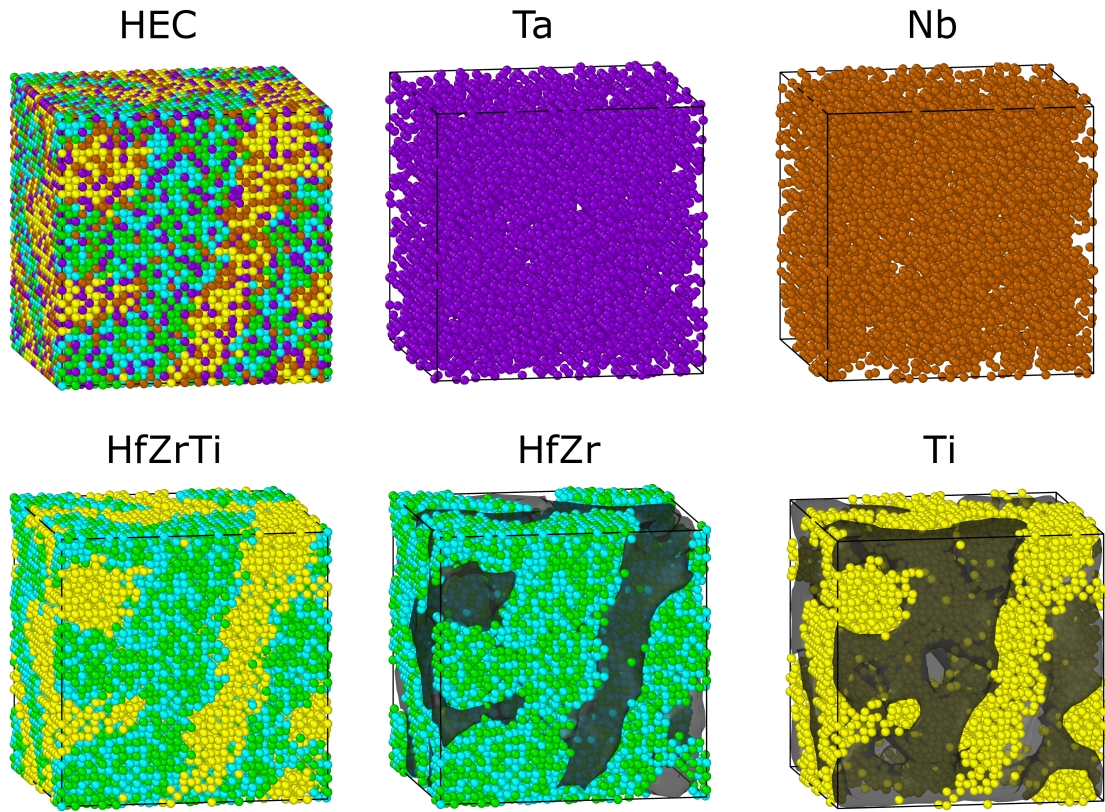


Figure 5-5: Simulated HEC containing 64000 atoms (32000 of metal atoms and 32000 carbons) at 500 K. Carbon atoms are not explicitly displayed here to make the distribution of metal atoms clearer. Immiscibility of TiC with HfC and ZrC is clearly seen, while NbC and TaC are perfectly mixed with all other carbides. Cavities where no carbides were observed except selected ones are shown by black color.

TiC samples was investigated. Specifically, the limiting factors for the formation of a fully mixed high-entropy carbide phase were studied. According to the results the main factor promoting the diffusion of metallic atoms is the formation of nearest-neighbor vacancy that can be occupied by diffusing atoms. In that case, the vacancy formation energies of host metallic atoms determine the diffusion rates and solubility of diffusing species in a host domain. Vacancy formation energies of five metals in the corresponding individual carbides, calculated with DFT, taken from work by Yu et al. [2015] are presented in Table 5.1. The cohesive energies of the corresponding pure metals were used as a chemical potential. As seen in the table, vacancy formation energies of metals in ZrC and HfC are almost three times higher

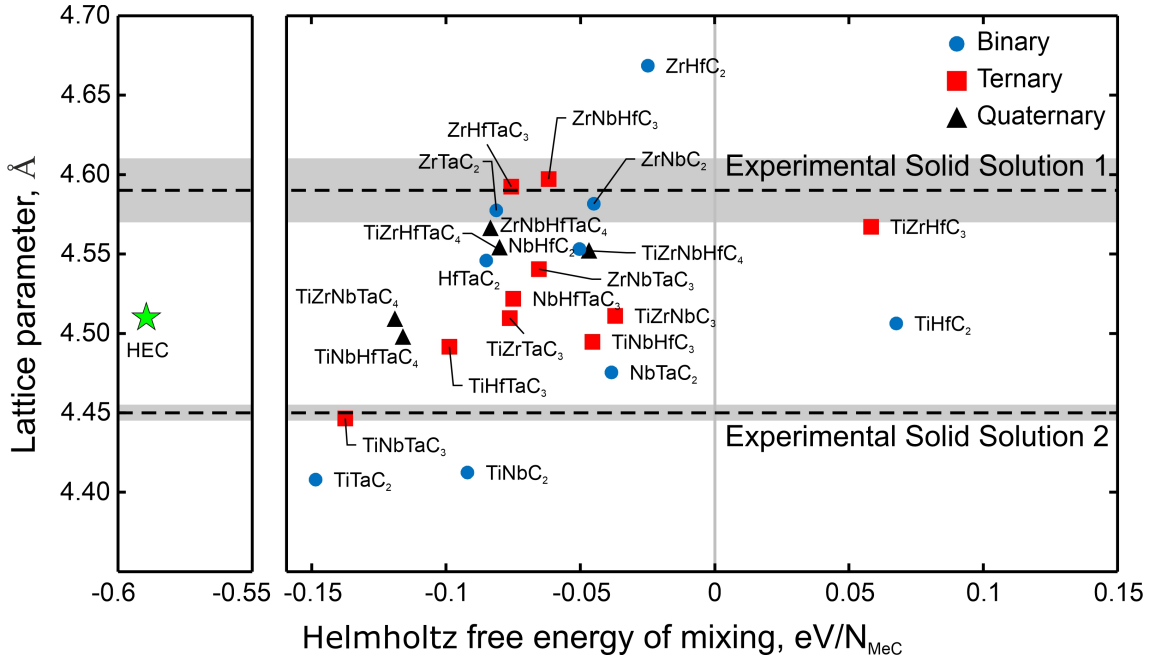


Figure 5-6: Correlation between the Helmholtz free energy of mixing as calculated at 500 K and the lattice parameters of binary (circles), ternary (squares), quaternary (triangles) carbides and HEC (star). Horizontal dashed lines and shaded areas represent lattice parameters and error of the experimentally observed phases respectively.

than that in TaC. That makes TaC to act as a host domain for inter-diffusion of Zr and Hf atoms, which drives the formation of (Zr-Hf-Ta)C phase. At the same time, vacancy formation of metals in TiC is almost two times higher than that in TaC, which more likely stimulates diffusion of ZrC and HfC into TaC-domain, rather than into TiC. As a consequence mixing of ZrC/HfC with TiC is not observed. Nb and Ti having higher vacancy formation energies can diffuse into TaC domain and form (Ti-Nb-Ta)C phase. On the contrary, due to lower vacancy formation energies of Nb and Ta, TiC tends to mix with NbC and TaC into a solid solution.

A proposed approach was for the first time applied to investigate phase-stability of high-entropy carbides. On the example of HfTaTiNbZrC_5 it was shown how the proposed method can predict a temperature of a solid solution formation and, consequently, guide the synthesis.

Element	Metal vacancy formation energy, eV Yu et al. [2015]
HfC	9.3
TaC	3.5
ZrC	9.4
NbC	4.1
TiC	8.6

Table 5.1: Vacancy formation energies of five metals in the corresponding individual carbides.

Chapter 6

Investigation of phase stability and short-range order of CrCoNi

The system under study represents a class of medium-entropy materials with $S_{\text{mix}} = 1.1R$. Practically, a reduced entropy contribution (in comparison with high-entropy alloys) can result in emergence of an atomic-scale short-range ordering (SRO) in the crystalline lattice of these materials. This can in principle impact thermodynamic stability as well as magnetic [Niu et al. \[2015\]](#) or mechanical properties [Zhang et al. \[2017\]](#). Therefore it is important to quantify the temperature-dependent ordering behaviour in this alloys.

A tendency for SRO in CrCoNi and its impact on thermodynamic quantities was already studied in several works. Evaluation of an experimental phase diagram revealed that equimolar CrCoNi forms a solid solution on a FCC lattice [Omori et al. \[2014\]](#). However, no information on possible SRO was provided. Further experimental investigations suggested different conclusions. For example, [Yin et al. \[2020\]](#) demonstrated that the strength and hardness of CrCoNi samples prepared under different annealing conditions, and hence with presumably different degrees of SRO, were not affected by the potential presence of SRO. However, another experimental investigation by [Zhang et al. \[2020\]](#) suggested a direct impact of SRO on the mechanical behaviour of this alloy.

The first computational investigation of SRO in CrCoNi was performed by [Tamm et al. \[2015\]](#), using first-principles based lattice Monte Carlo simula-

tions. The results showed an increase of Cr-Co and Cr-Ni nearest-neighbors at the expense of Cr-Cr pairs. The observed Cr-Cr repulsion was explained by a magnetic frustration. Another computational study using cluster expansion was performed by Pei et al. [2020]. The proposed FCC ground state structure had alternating Cr rich layers and mixed Co and Ni atoms layers. However, the energy difference of around 31 meV/atom between the random structure and the proposed ground state is smaller than the energy difference of around 45 meV/atom reported by Tamm et al. [2015]. This may suggest the existence of another ground state structure.

Though several experimental and theoretical studies were performed to reveal the impact of SRO on phase stability of CrCoNi, some discrepancies still exist. In the present work an on-lattice Monte Carlo combined with LRP is used to investigate SRO in CrCoNi over a wide temperature window. Based on the simulation results, SRO impact on a phase stability and the role of magnetism for it is analyzed.

6.1 Calculation details

To train the LRP, the algorithm, presented in Fig. 3-8 was employed. The initial dataset contained 600 random configurations, each with 108 atoms. After performing Monte Carlo simulations 780 additional configurations were sampled, recalculated with DFT and added to the initial dataset. Thus, the final set contained 1380 configurations and was split into training and validation subsets of 1180 and 200 configurations respectively. The RMSE on the validation subset was 2.36 meV/atom.

The reference energies were calculated using spin-polarized DFT as implemented in VASP 5.3.5 Kresse and Furthmüller [1996], Kresse and Hafner [1993, 1994]. A projector augmented wave (PAW) method Blöchl [1994] utilizing the Perdew-Burke-Ernzerhof generalized gradient approximation (PBE-GGA) Perdew et al. [1996] was employed. A lattice parameter of 3.55 Å was used, which corresponds to experimentally observed lattice constant Tamm et al. [2015], Ding et al. [2018]. The plane-wave energy cutoff was set to 300 eV. For the considered $3 \times 3 \times 3$ (108 atom) supercell an energy cut off of 300 eV and a Monkhorst-Pack Monkhorst and Pack [1976] $4 \times 4 \times 4$ k-mesh was used for the self-consistent calculations. The convergence

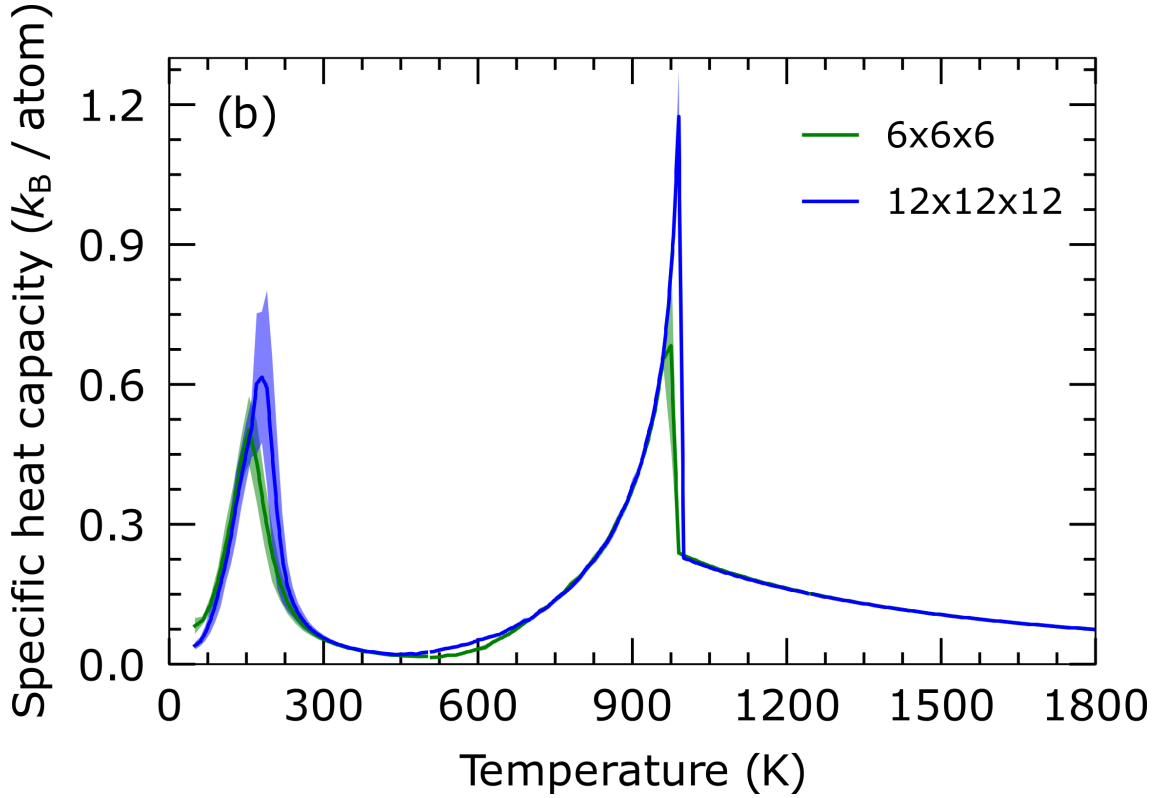


Figure 6-1: Specific heat capacity $C_V(T)$ for *fcc* CrCoNi from CMC simulations for a $6 \times 6 \times 6$ and $12 \times 12 \times 12$ simulation box.

criteria for total energies was set to 10^{-3} eV. To include magnetism, each calculated configuration was initialized with different random arrangements of magnetic spins.

6.2 Results of CrCoNi study

Using CMC simulations, temperature dependent specific heat capacity was calculated in a range between 0 K and 1800 K. To assess the generalization ability of the LRP, simulations were performed for two supercells with sizes $6 \times 6 \times 6$ (864 atoms) and $12 \times 12 \times 12$ (6912 atoms). The results are presented on Fig. 6-1. Two characteristic peaks revealing two possible phase transitions are observed. A first transition is found around 180 K, and the second around 975 K. Notably, the observed peak around 975 K is in a good agreement with the previous experimental observations at the corresponding temperature Jin et al. [2017]. As seen, increasing the supercell size from $6 \times 6 \times 6$ to $12 \times 12 \times 12$ results only in insignificant

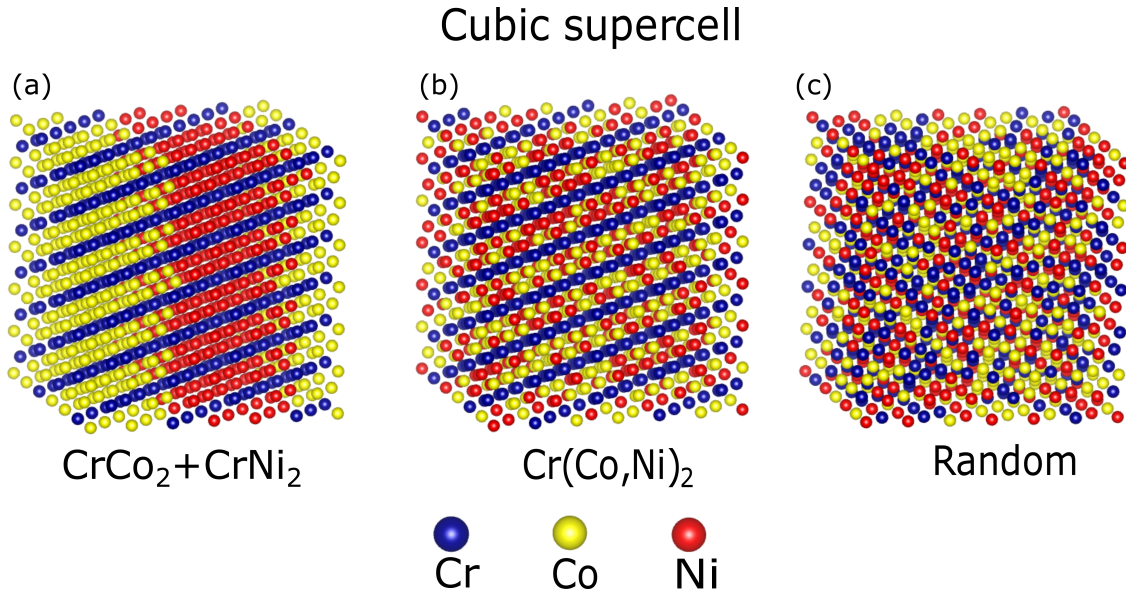


Figure 6-2: Simulated structures. (a) CrCo₂+CrNi₂ obtained at 50 K. (b) Cr(Co,Ni)₂ obtained at 510 K. (c) Random solid solution obtained at very high temperature.

changes in the heat capacity values. Therefore, the subsequent analysis was based on $12 \times 12 \times 12$ supercell size calculations.

Three characteristic configurations for the different temperature regimes are shown in Fig. 6-2. First, a low-temperature (50 K) configuration, separated into CrCo₂ and CrNi₂ is presented (Fig. 6-2a). The second, obtained at 510 K., is an ordered structured referred to as Cr(Co,Ni)₂ (Fig. 6-2b). And the last, shown on Fig. 6-2c, is a random solid solution phase obtained at very high temperature.

Next, an ordering behavior was analyzed. To quantify the degree of ordering, the Warren-Cowley SRO parameters Cowley [1960] were calculated as,

$$\alpha_{ij}^m = 1 - \frac{p_{ij}^m}{c_i c_j}, \quad (6.1)$$

where α_{ij}^m is the Warren-Cowley SRO parameter for the atomic types i and j at the m^{th} coordination shell; p_{ij}^m is the probability of finding atom type j at the m^{th} coordination shell of atom i , and c_i , c_j are the concentrations of elements i and j in the alloy. Positive (negative) values of the SRO parameter at the m^{th} coordination

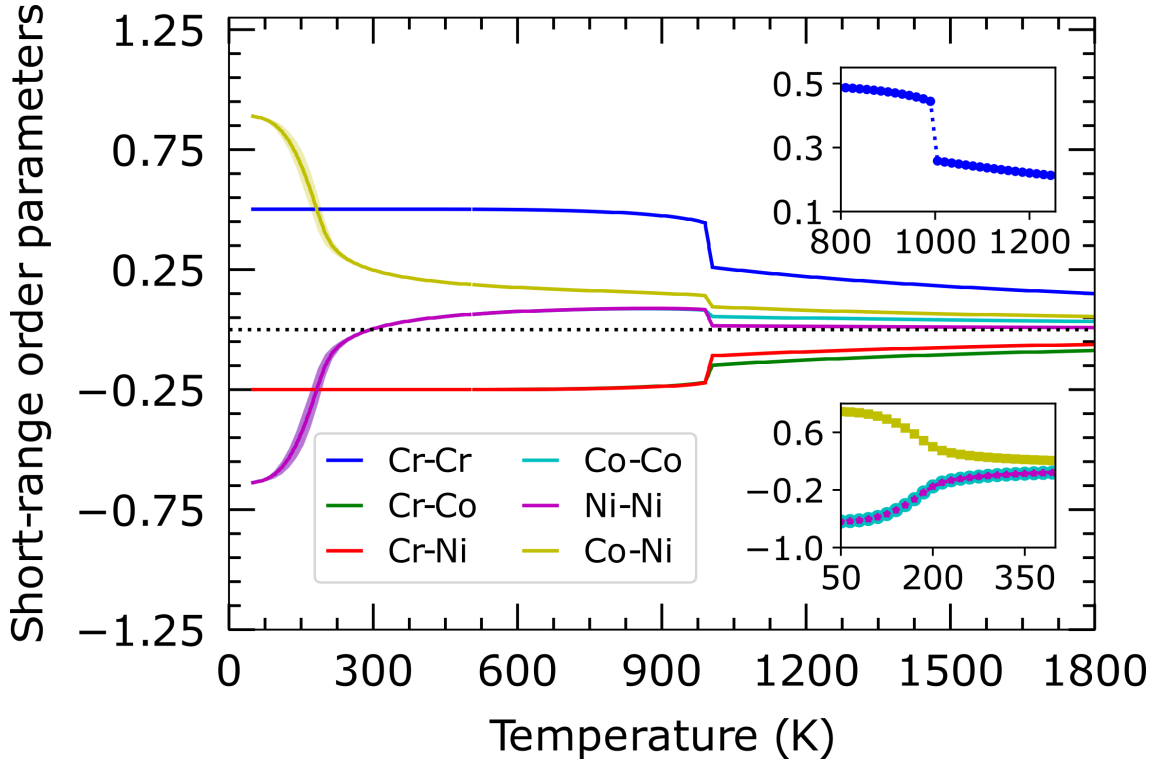


Figure 6-3: Temperature-dependent Warren-Cowley SRO parameters for different atom pairs in the first coordination shell in CrCoNi alloy. The panels demonstrate qualitatively different nature of the low- and high-temperature transitions.

shell indicate repulsion (attraction) between atoms i and j at the corresponding coordination shell. Dependence of Warren-Cowley SRO parameter on temperature for different atomic pairs in the first coordination shell is shown on Fig. 6-3. At temperatures above 975 K, a positive value of $\alpha_{\text{Cr-Cr}}$ indicates Cr-Cr repulsion, while negative values of $\alpha_{\text{Cr-(Co, Ni)}}$ indicates a preference for Cr to form a bond with Co and Ni. Nevertheless, $\alpha_{\text{Cr-Cr}}$ and $\alpha_{\text{Cr-(Co, Ni)}}$ are close to zero, which reflects a some degree of randomness in Co and Ni distribution in an alloy. The tendency of Cr to bond with Co and Ni becomes more prominent below the high-temperature transition around 975 K. As it is seen $\alpha_{\text{Cr-(Co, Ni)}}$ becomes more negative, which indicates an increase of SRO driven by Cr-Co and Cr-Ni bonds. On the contrary $\alpha_{\text{Cr-Cr}}$ shows an abrupt increase, which reflects a higher repulsion between Cr atoms. This trend is consistent with the ordered $\text{Cr}(\text{Co, Ni})_2$ structure observed as shown in Fig. 6-2b. Further, at temperatures below 300 K $\alpha_{\text{Cr-Cr}}$ value saturates at a value of 0.5 and $\alpha_{\text{Ni-Ni}}$ becomes strongly negative, thus supporting the low temperature

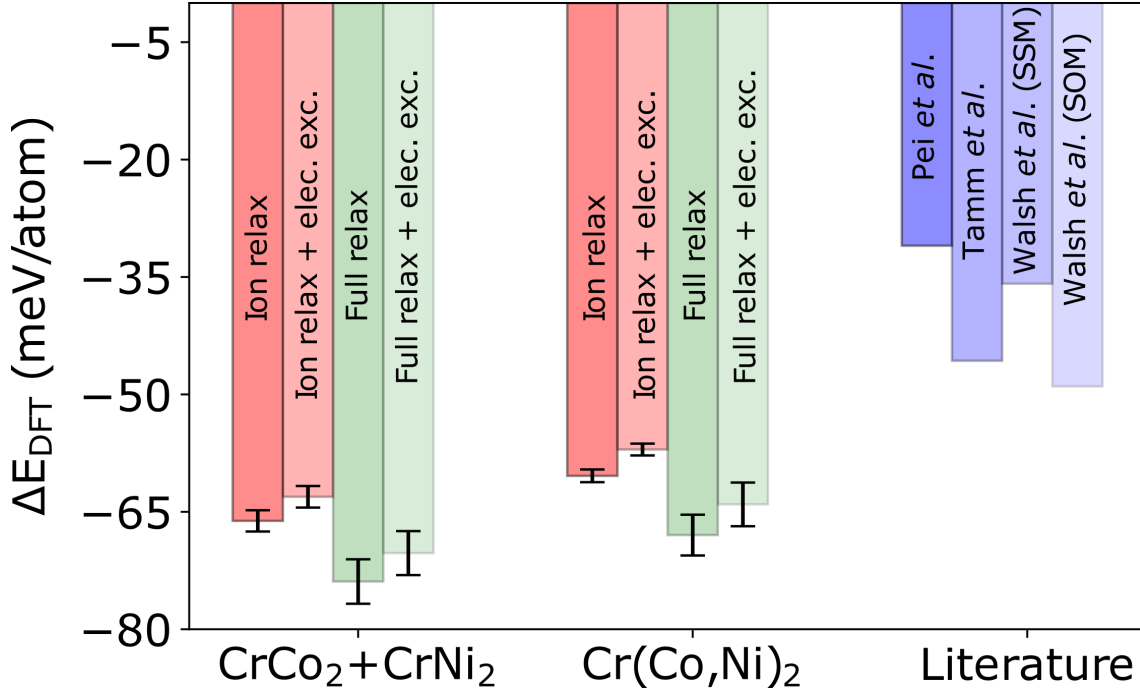


Figure 6-4: DFT calculated energy differences as compared to a random alloy for the two ordered states found in the present work as well as previous works. The calculations include purely ionic relaxations (red) as well as full relaxation (green). The impact of electronic excitations (light red and light green) are shown as well. The DFT calculated energy differences found in previous works (blue shades) by Pei et al. [2020], Tamm et al. [2015] and Walsh et al. [2021] between the random alloy and there proposed ordered state have been also added.

separation of CrCoNi into CrCo₂+CrNi₂.

Such results lead to a conclusion that the high-temperature phase transition reflected in the peak in the specific heat capacity curve at 975 K is mainly driven by the ordering of the Cr atoms. The low-temperature phase transition, reflected in the second peak, is clearly driven by the ordering of Co and Ni. A good agreement between the computed SRO of the ordered configuration (at 500 K) and experimental findings was obtained as shown in Tab. 6.1.

Although the calculated SRO parameters qualitatively agree with the previous works, some discrepancies are observed comparing the energy differences of an ordered structure with the random solid solution. The ordered configuration suggested in Pei et al. [2020] is about 31 meV/atom lower in energy as compared to the random one, while Tamm et al. [2015] an energy difference of 45.7 meV/atom at 500 K.

This suggests that the ordered configuration proposed in Pei et al. [2020] is likely not the energetically most favorable one. To compare findings of this work with the mentioned studies all of the three structures (depicted in Fig. 6-2) were recalculated using DFT. To account for a statistical divergence, DFT calculations were performed for 30 configurations, sampled from CMC simulation, for each case ($\text{CrCo}_2+\text{CrNi}_2$, $\text{Cr}(\text{Co,Ni})_2$ and random). All energy differences for $\text{CrCo}_2+\text{CrNi}_2$ and $\text{Cr}(\text{Co,Ni})_2$ structures with respect to the random one are shown in Fig. 6-4 and compared to those of the ordered phases proposed in the literature. The error bars indicate the standard deviation for the averaged computed DFT values for each case. The impact of a volume relaxation as well as the inclusion of electronic excitations was also studied. As it is evident, for every considered scenario the ordered $\text{Cr}(\text{Co,Ni})_2$ structure, proposed in this work, is found to be significantly lower in comparison with previous results.

To rationalize the reason behind the energetic difference the proposed ordered structure was analyzed and compared to the one reported in literature. Both structures are shown in Fig. 6-5. As shown in Fig. 6-5(c), a ground state ordered structure suggested by Pei et al. [2020] have a $\{002\}$ layer completely occupied by Cr and Ni and Co sharing the other two layers in a period of three layers. An almost identical tendency in arrangement of atomic layers is observed in ordered structure obtained in this work (see Fig. 6-2(b)). Again a layer, completely occupied by Cr, followed by two layers with mixed Co and Ni atoms as shown for both supercell types. However, the remarkable difference between both configurations is that in contrast to Fig. 6-5 (c), in Fig. 6-5(a) and (b) each Cr bonds only with two nearest neighbour Cr atoms, which is consistent with the saturated value of $\alpha_{\text{Cr-Cr}}$ in Fig. 6-3 This

Table 6.1: Presently calculated low rank potentials (LRP) based Monte Carlo (MC) simulated Warren-Cowley SRO parameters in CrCoNi alloy at a temperature of 500 K compared to previous DFT based Monte Carlo studies by Tamm et al. [2015] and Ding et al. [2018].

Neighbor atoms pair	Present calculation LRP MC	Tamm et al. [2015] DFT MC	Ding et al. [2018] DFT MC
Cr-Cr	0.50	0.42	0.40
Cr-Co	-0.25	-0.16	-0.25
Cr-Ni	-0.25	-0.27	-0.15
Co-Co	0.06	0.01	0.06
Ni-Ni	0.06	0.12	-0.04
Co-Ni	0.19	0.15	0.19

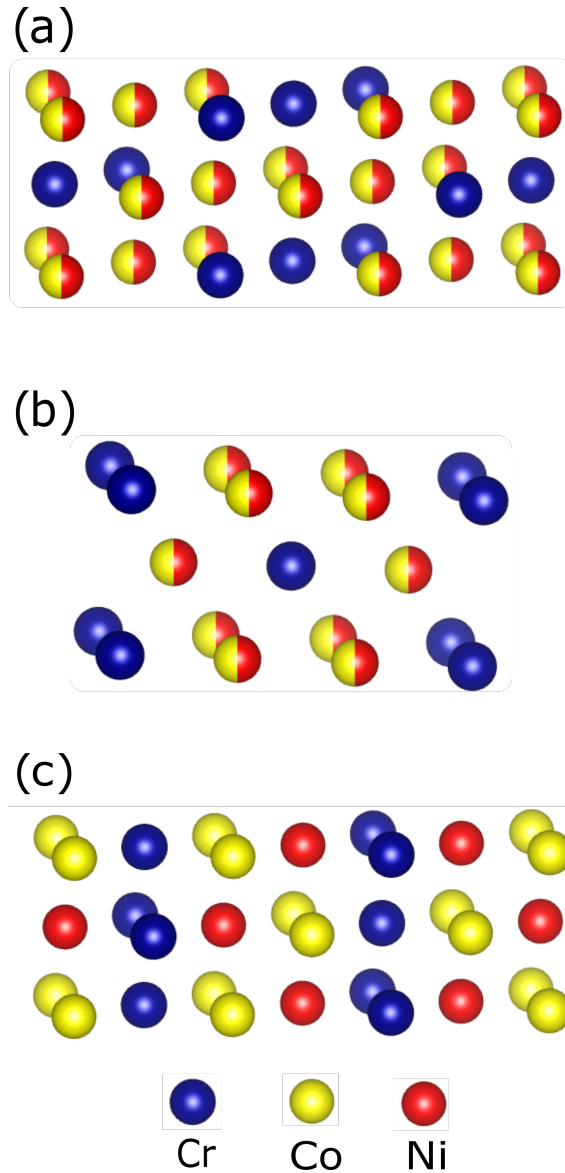


Figure 6-5: The arrangement of constituent atoms in (a) the presently obtained ordered structure (in case of cubic supercell) of CrCoNi at a temperature of 510 K compared with (c) the ground state structure as suggested by Pei et al. [2020]. In case of (a), for clear visualization of our obtained Cr(Co,Ni)₂ structure, only a certain part of the 864-atom cell with smaller boundary is shown. Another orthorhombic primitive cell as considered in case of orthorhombic supercell for Cr(Co,Ni)₂ structure has been also added in (b) for better visualization. The half-coloured spheres with yellow and red represents the 50% occupancy probability of Co and Ni for those sites.

may favor magnetic contributions as previous investigations on CrCoNi suggested that the frustration of antiferromagnetic Cr can be greatly relieved by minimizing the amount of Cr–Cr nearest neighbors.

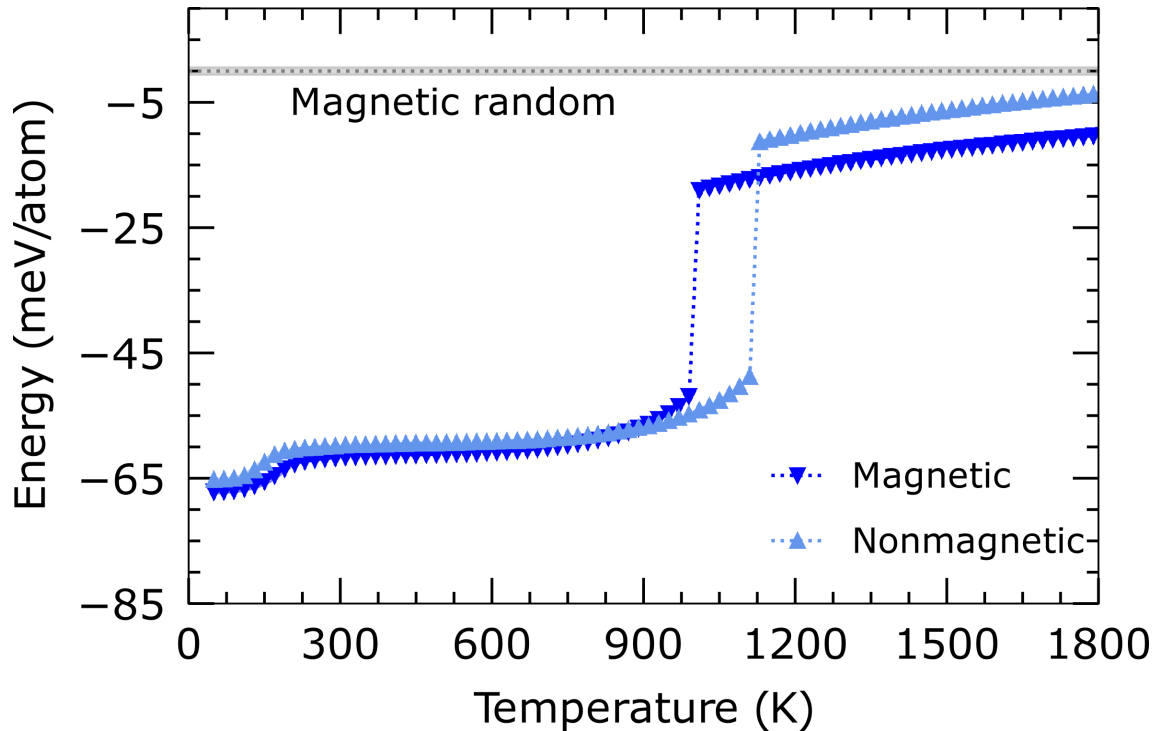


Figure 6-6: The calculated temperature dependence of mean internal energies obtained from magnetic and non-magnetic LRP based MC simulations for equiatomic CrCoNi alloy with supercell size $12 \times 12 \times 12$. The energy of high temperature magnetic random solid solution has been included as reference (grey line).

Further, the magnetic contribution into ordering behavior is investigated. To do so, a separate simulation with excluded magnetic degrees of freedom were performed. The whole procedure of preparing training and validation sets was repeated with non-spin polarized DFT and a new LRP was obtained (here and further LRP fitted to non-spin polarized DFT is called “non-magnetic”; to spin-polarized DFT - “magnetic”). Further, the ordering in the system was investigated by performing CMC simulation with LRP trained on non-spin polarized calculations. The temperature dependency of mean total energy obtained in MC simulation is shown in Fig. 6-6 in comparison with the previous magnetic calculation. Evidently, the total energy remains almost the same in the ordered region below 900 K, though with a slight shift in the transition temperature. The ordering trend in the observed structure remained exactly the same as obtained from spin-polarized calculations. Therefore, magnetism is actually not responsible for the ordering behavior.

The proposed approach was applied to investigate phase-stability and SRO in

CrCoNi alloy. It was revealed that magnetism does not play a leading role in ordering behavior and SRO is mainly driven by the chemical arrangement of atoms. Moreover, it was shown for the first time that LRP is capable to implicitly account for magnetic degrees of freedom.

Chapter 7

Conclusion

In this thesis I developed an approach for the design of multicomponent materials using the on-lattice modeling. Lattice-based simulations were applied to two problems of multicomponents materials design, namely, crystal structure prediction and modeling of phase stability at finite temperatures. To solve these tasks I developed two separate methods both based on on-lattice structure generation algorithm and on-lattice machine-learning interatomic potentials. A conceptually new crystal structure prediction method, called on-lattice CSP, was developed. Unlike state-of-art CSP algorithms, on-lattice CSP generates the structure iteratively, adding atom by atom in the sites of the lattice. The algorithm produces population of structures with all possible types of atoms on a chosen site, and selects the structure with the lowest energy. Thus, by using a “smart” generation approach, combined with the LRP or CE, on-lattice CSP discover configurations with different chemical composition and, preferably, closer to the convex hull. For modeling the phase stability I used on-lattice CMC simulations with the LRP. In this work it was shown that this method can also be applied to the study of high-entropy carbides and reveal the impact of magnetism on the SRO in MEA. By using the LRP/CE as an interaction model, the number of required DFT calculations was substantially reduced to an amount sufficient for constructing a training set only. The approach proposed was implemented in a software package based on C++ backend and Python user interface.

First, the developed methodology was applied to discover stable compounds in

Nb-Mo-Ta-W system. Using on-lattice CSP I constructed binary Nb-W, ternary Mo-Ta-W, and quaternary Nb-Mo-Ta-W convex hulls. The obtained results were compared to those present in the AFLOW database. The algorithm has discovered 9 new binaries (Nb_3W_4 , NbW_2 , Nb_3W_7 , NbW_4 , NbW_5 , NbW_8 , TaW_8 , TaMo_5 , TaMo_6) and 3 new ternaries ($\text{Mo}_3\text{Ta}_3\text{W}$, MoTa_2W_2 and MoTaW_5). Also, two new quaternary alloys were discovered - NbMoTaW_6 and $\text{NbMo}_2\text{TaW}_{18}$. The results demonstrate that the developed structure generation algorithm, combined with the LRP and CE models, can substantially accelerate the search. Only a few hundred DFT calculations were required to discover new compounds as well as the previously reported in the literature.

In the next work the on-lattice CMC with the LRP was applied to study phase stability of HfTaTiNbZrC_5 high-entropy carbide. The results of the simulations were used to guide the subsequent synthesis. The simulations revealed the presence of a solid solution phase at temperatures above 1200 K. At ambient temperatures a phase decomposition was observed. At 500 K the sample decomposes into random $(\text{Ti-Nb-Ta})\text{C}$ and $(\text{Zr-Hf-Ta})\text{C}$ and phases. To obtain the corresponding samples, the parameters of the arc plasma reactor were adjusted to provide the temperatures, predicted in the simulations. The experimental results are in an excellent agreement with the theory, which is evident from the provided XRD diagrams and SEM images.

Finally, the on-lattice CMC with the LRP was applied to investigate the SRO and phase stability of CrCoNi alloy. The simulations revealed a lower energy ordering as compared to the structures reported in the literature [Tamm et al. \[2015\]](#), [Pei et al. \[2020\]](#). The observed SRO is mainly driven by Cr-Ni and Cr-Co pairs. The structure obtained is almost identical to the one, reported by [Pei et al. \[2020\]](#), though with a fewer number of Cr-Cr nearest-neighbors. Such ordering can be caused by a relief of magnetic frustration effects. To investigate the impact of magnetic frustration on the SRO additional CMC simulations were performed. This time the LRP was trained on non-spin polarized DFT calculations. Eventually, the same ordering behavior was observed, which reveals the minor impact of magnetism on the SRO.

The results presented in this work demonstrate the effectiveness of on-lattice modeling in designing multicomponent materials. First, it was demonstrated that

on-lattice structure generation algorithms can sample multicomponent configurational space with reduced computational costs. Second, the sampling was performed in a high-throughput manner by using machine-learning interatomic potentials. As a result, the number of required DFT calculations was reduced to the order of several hundreds. The developed methodology also has a practical significance. In particular, as demonstrated in the second work, the simulations can assist the controllable synthesis of materials. Thus, the developed tools also shorten the gap between theoretical and experimental design of materials.

Chapter 8

Appendix

8.1 Technical realization of “on-lattice” package

The methodology described was implemented in a stand alone “on-lattice” package using C++ and Python programming languages. It can be accessed via GitLab upon the request (<https://gitlab.com/ashapeev/on-lattice-structure-prediction>).

The developed code has three levels as shown on Fig. 8-1 The first one is a core level, that contains C++ modules. This level in turn, consists of two sub-levels. The first sub-level contain two modules: `cfg.h` that is responsible for performing manipulations with atomic structure (creating configuration with different crystal lattices, sizes, chemical elements, etc.), and `pot.h` that contains technical realization of LRP and CE. The second sub-level consists of `cmc-simulation.h` and `structure-prediction.h` modules with technical realization of on-lattice Monte Carlo and on-lattice-CSP.

The second level, called “wrapper”, is an intermediate level, written in Cython. It is used to wrap C++ modules (using `.pyx` files) and connect them with the Python user interface. The last level, is a Python-written user interface that is used to perform the simulations, obtain and analyze the results.

Module `cfg.h` contains classes `Lattice` and `Configuration`. Class `Lattice` is used to create a lattice object, that holds information about lattice type (bcc, fcc, etc.). To initialize the lattice object the following parameters are passed to constructor:

1. `cell` - matrix with coordinates of a unit cell vector
2. `shifts` - matrix with coordinates of a subcell origin.

The attributes of the class are the following:

1. `neighbors` - matrix with coordinates of nearest-neighbors including the central cite.
2. `n_neighbors` - number of nearest-neighbors including the central cite.

To create the object of class `Configuration` the following parameters are provided as input:

1. `lattice` - object of class `Lattice`.
2. `shape` - matrix that defines the size of configuration.
3. `occupancy` - vector with atomic numbers of length equal to the number of sites.

Module `pot.h` contains classes `PotCE` and `PotLRP` that are used to created objects of CE and LRP potentials. Modules `cmc_simulation.h` and `csp_simulation.h` contain classes `CMC_Simulation` and `CSP_Simulation` respectively. To create objects of this classes the following arguments should be passed:

1. `pot` - object of `PotCE` class or `PotLRP` class. Represents the potential used in the simulation.
2. `cfg` - object of `Configuration`. Represents the initial configuration.

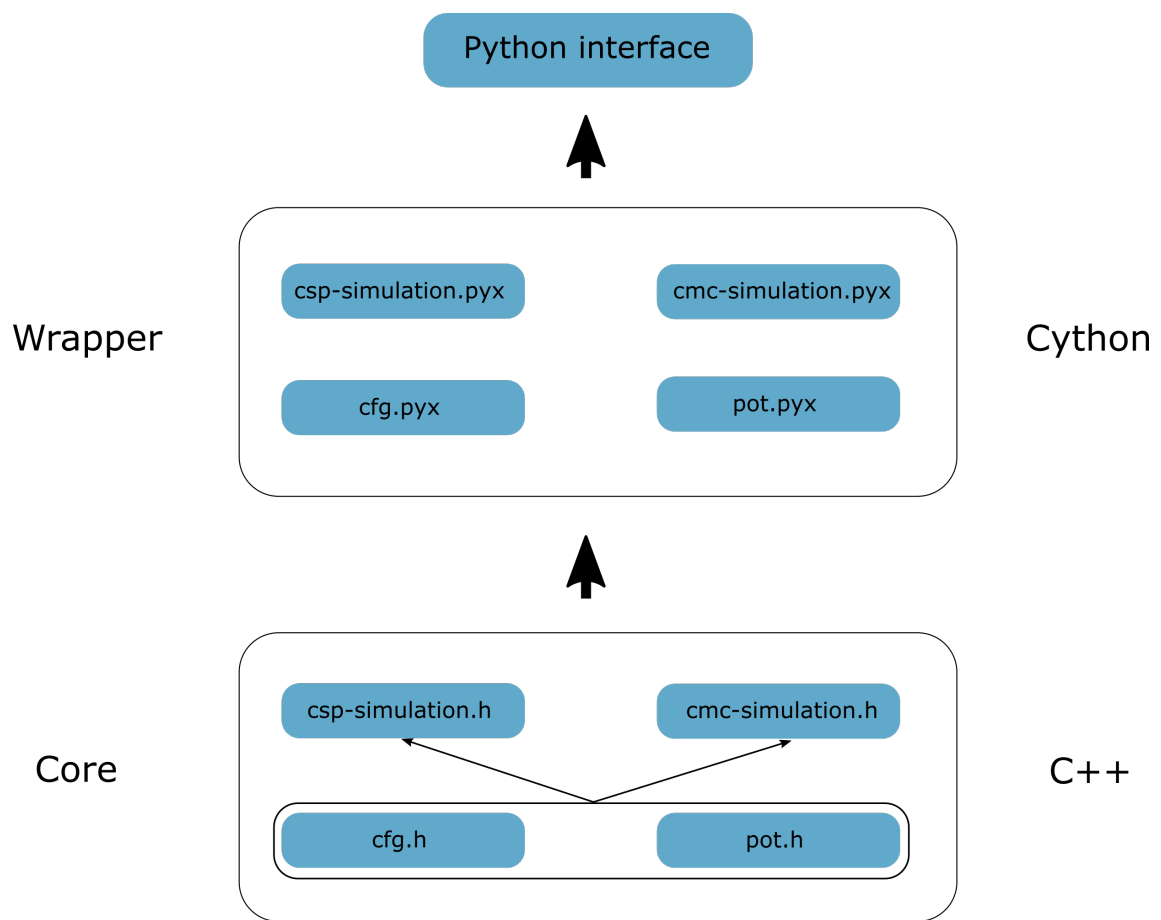


Figure 8-1: Structure of the developed code.

Bibliography

- Ali Abd El-Aty, Yong Xu, Shihong Zhang, Yan Ma, and Dayong Chen. Experimental investigation of tensile properties and anisotropy of 1420, 8090 and 2060 al-li alloys sheet undergoing different strain rates and fibre orientation: a comparative study. *Procedia Engineering*, 207:13–18, 2017.
- Albert P. Bartók, Mike C. Payne, Risi Kondor, and Gábor Csányi. Gaussian approximation potentials: The accuracy of quantum mechanics, without the electrons. *Phys. Rev. Lett.*, 104:136403, 2010.
- F. Bechstedt. *Born-Oppenheimer Approximation*, pages 3–11. 12 2015. ISBN 978-3-662-44592-1. doi:[10.1007/978-3-662-44593-8_1](https://doi.org/10.1007/978-3-662-44593-8_1).
- Jörg Behler and Michele Parrinello. Generalized neural-network representation of high-dimensional potential-energy surfaces. *Phys. Rev. Lett.*, 98:146401, 2007.
- P. E. Blöchl. Projector augmented-wave method. *Phys. Rev. B*, 50:17953–17979, 1994.
- B. Cantor, I.T.H. Chang, P. Knight, and A.J.B. Vincent. Microstructural development in equiatomic multicomponent alloys. *Materials Science and Engineering: A*, 375-377:213–218, 2004.
- Brian Cantor. Multicomponent and high entropy alloys. *Entropy*, 16(9):4749–4768, 2014.
- Elinor G Castle, Tamás Csanádi, Salvatore Grasso, Ján Dusza, and Mike Reece. Processing and properties of high-entropy ultra-high temperature carbides. *Scientific Reports*, 8, 2018.
- Lucian A. Constantin, E. Fabiano, and F. Della Sala. Improving atomization energies of molecules and solids with a spin-dependent gradient correction from one-electron density analysis. *Phys. Rev. B*, 84:233103, 2011.
- J. M. Cowley. Short- and long-range order parameters in disordered solid solutions. *Phys. Rev.*, 120:1648–1657, 1960.
- Stefano Curtarolo, Wahyu Setyawan, Gus L.W. Hart, Michal Jahnatek, Roman V. Chepulskii, Richard H. Taylor, Shidong Wang, Junkai Xue, Kesong Yang, Ohad Levy, Michael J. Mehl, Harold T. Stokes, Denis O. Demchenko, and Dane Morgan. Aflow: An automatic framework for high-throughput materials discovery. *Computational Materials Science*, 58:218–226, 2012. ISSN 0927-0256.

- D. Demirskyi, T.S. Suzuki, K. Yoshimi, and O. Vasylykiv. Synthesis and high-temperature properties of medium-entropy (ti,ta,zr,nb)c using the spark plasma consolidation of carbide powders. *Open Ceramics*, 2:100015, 2020.
- Lin Deye, S. S. Wang, D. L. Peng, X. D. Hui, and M. Li. An n-body potential for a zr–nb system based on the embedded-atom method. *Journal of Physics Condensed Matter*, 25(10):14, Mar 2013.
- Jun Ding, Qin Yu, Mark Asta, and Robert O. Ritchie. Tunable stacking fault energies by tailoring local chemical order in crconi medium-entropy alloys. *Proceedings of the National Academy of Sciences*, 115(36):8919–8924, 2018.
- Baojuan Dong, Zhenhai Wang, Nguyen T. Hung, Artem R. Oganov, Teng Yang, Rii-ichiro Saito, and Zhidong Zhang. New two-dimensional phase of tin chalcogenides: Candidates for high-performance thermoelectric materials. *Phys. Rev. Mater.*, 3: 013405, 2019a.
- Huafeng Dong, Artem R. Oganov, Vadim V. Brazhkin, Qinggao Wang, Jin Zhang, M. Mahdi Davari Esfahani, Xiang-Feng Zhou, Fugen Wu, and Qiang Zhu. Boron oxides under pressure: Prediction of the hardest oxides. *Phys. Rev. B*, 98:174109, Nov 2018.
- Xiao Dong, Jingyu Hou, Jun Kong, Haixu Cui, Yan-Ling Li, Artem R. Oganov, Kuo Li, Haiyan Zheng, Xiang-Feng Zhou, and Hui-Tian Wang. Predicted lithium oxide compounds and superconducting low-pressure lio_4 . *Phys. Rev. B*, 100:144104, Oct 2019b.
- Easo P. George, Dierk Raabe, and Robert O. Ritchie. High-entropy alloys. *Nature Reviews Materials*, 4(8):515–534, 2019.
- Sheuly Ghosh, Vadim Sotnikov, Alexander V. Shapeev, Jörg Neugebauer, and Fritz Körmann. Short-range order and phase stability of crconi explored with machine learning potentials. *Phys. Rev. Mater.*, 6:113804, 2022.
- Colin W. Glass, Artem R. Oganov, and Nikolaus Hansen. Uspex - evolutionary crystal structure prediction. *Comput. Phys. Commun.*, 175:713–720, 2006. URL <https://api.semanticscholar.org/CorpusID:939023>.
- Blazej Grabowski and Nikolay Zotov. Thermally-activated dislocation mobility in bcc metals: An accelerated molecular dynamics study. *Computational Materials Science*, 200:110804, 2021.
- Konstantin Gubaev, Evgeny V. Podryabinkin, Gus L.W. Hart, and Alexander V. Shapeev. Accelerating high-throughput searches for new alloys with active learning of interatomic potentials. *Computational Materials Science*, 156:148–156, 2019.
- Sheng Guo, Chun Ng, Jian Lu, and C. Liu. Effect of valence electron concentration on stability of fcc or bcc phase in high entropy alloys. *Journal of Applied Physics*, 109, 05 2011.

- J. H. A. Hagelaar, E. Bitzek, C. F. J. Flipse, and P. Gumbsch. Atomistic simulations of the formation and destruction of nanoindentation contacts in tungsten. *Phys. Rev. B*, 73:045425, 2006.
- D. R. Hamann. Generalized gradient theory for silica phase transitions. *Phys. Rev. Lett.*, 76:660–663, 1996.
- B. Hammer, K. W. Jacobsen, and J. K. Nørskov. Role of nonlocal exchange correlation in activated adsorption. *Phys. Rev. Lett.*, 70:3971–3974, 1993.
- Vincent H. Hammond, Mark A. Atwater, Kristopher A. Darling, Hoang Q. Nguyen, and Laszlo J. Kecskes. Equal-channel angular extrusion of a low-density high-entropy alloy produced by high-energy cryogenic mechanical alloying. *JOM*, 66(10):2021–2029, 2014.
- Gus L. W. Hart and Rodney W. Forcade. Algorithm for generating derivative structures. *Phys. Rev. B*, 77:224115, 2008.
- Gus L. W. Hart and Rodney W. Forcade. Generating derivative structures from multilattices: Algorithm and application to hcp alloys. *Phys. Rev. B*, 80:014120, 2009.
- Gus L.W. Hart, Lance J. Nelson, and Rodney W. Forcade. Generating derivative structures at a fixed concentration. *Computational Materials Science*, 59:101–107, 2012.
- M. Hodapp, G. Ancaux, J.-F. Molinari, and W.A. Curtin. Coupled atomistic/discrete dislocation method in 3d part ii: Validation of the method. *Journal of the Mechanics and Physics of Solids*, 119:1–19, 2018.
- Da Hong, Hebin Wang, Longgang Hou, Ping Ou, Yiqi Wang, and Hongjin Zhao. Effect of aging treatment on microstructure and properties of the fe55(cocrni)10(mov)5c5 medium-entropy alloy. *Metals*, 10(8), 2020.
- M.D. Hossain, T. Borman, A. Kumar, X. Chen, A. Khosravani, S.R. Kalidindi, E.A. Paisley, M. Esters, C. Oses, C. Toher, S. Curtarolo, J.M. LeBeau, D. Brenner, and J-P Maria. Carbon stoichiometry and mechanical properties of high entropy carbides. *Acta Materialia*, 215:117051, 2021.
- Frank Jensen. Introduction to computational chemistry. chapter 3, pages 87–92. John Wiley & Sons, 2007a.
- Frank Jensen. Introduction to computational chemistry. chapter 4, pages 133–189. John Wiley & Sons, 2007b.
- Frank Jensen. Introduction to computational chemistry. chapter 6, pages 232–264. John Wiley & Sons, 2007c.
- Frank Jensen. Introduction to computational chemistry. chapter 2, pages 22–77. John Wiley & Sons, 2007d.

- K. Jin, S. Mu, K. An, W.D. Porter, G.D. Samolyuk, G.M. Stocks, and H. Bei. Thermophysical properties of ni-containing single-phase concentrated solid solution alloys. *Materials & Design*, 117:185–192, 2017.
- G. Kern, G. Kresse, and J. Hafner. Ab initio calculation of the lattice dynamics and phase diagram of boron nitride. *Phys. Rev. B*, 59:8551–8559, 1999.
- Evan Kiely, Reabetswe Zwane, Robert Fox, Anthony M. Reilly, and Sarah Guerin. Density functional theory predictions of the mechanical properties of crystalline materials. *CrystEngComm*, 23:5697–5710, 2021.
- Tsz Wai Ko, Jonas A. Finkler, Stefan Goedecker, and Jörg Behler. A fourth-generation high-dimensional neural network potential with accurate electrostatics including non-local charge transfer. *Nature Communications*, 12(1):398, 2021.
- Tatiana Kostiuchenko, Fritz Koermann, Joerg Neugebauer, and Alexander Shapeev. Impact of lattice relaxations on phase transitions in a high-entropy alloy studied by machine-learning potentials. *npj Computational Materials*, 5:55, 2019.
- Tatiana Kostiuchenko, Andrei V Ruban, Jörg Neugebauer, Alexander Shapeev, and Fritz Körmann. Short-range order in face-centered cubic vconi alloys. *Physical Review Materials*, 4(11):113802, 2020.
- G. Kresse and J. Furthmüller. Efficient iterative schemes for ab initio total-energy calculations using a plane-wave basis set. *Phys. Rev. B*, 54:11169–11186, 1996.
- G. Kresse and J. Hafner. Ab initio molecular dynamics for liquid metals. *Phys. Rev. B*, 47:558–561, 1993.
- G. Kresse and J. Hafner. Ab initio molecular-dynamics simulation of the liquid-metal–amorphous-semiconductor transition in germanium. *Phys. Rev. B*, 49:14251–14269, 1994.
- EJ Lavernia, Tirumalai S Srivatsan, and FA Mohamed. Strength, deformation, fracture behaviour and ductility of aluminium-lithium alloys. *Journal of Materials Science*, 25:1137–1158, 1990.
- Sangjun Lee, Heon Kang, and Donghyun Bae. Molecular dynamics study on crack propagation in al containing mg–si clusters formed during natural aging. *Materials*, 16(2), 2023.
- Zhongtao Li, Zhe Wang, Zhenggang Wu, Biao Xu, Shijun Zhao, Weidong Zhang, and Nan Lin. Phase, microstructure and related mechanical properties of a series of (nbtazr)c-based high entropy ceramics. *Ceramics International*, 47(10, Part A):14341–14347, 2021.
- Andriy O. Lyakhov, Artem R. Oganov, Harold T. Stokes, and Qiang Zhu. New developments in evolutionary structure prediction algorithm uspx. *Computer Physics Communications*, 184(4):1172–1182, 2013.

- Stavroula Maritsa, Spyridon Chaskis, Paul Stavroulakis, Sofia Papadopoulou, Russell Goodall, and Spyros Papaefthymiou. Casting and study of thermal processes in copper-based multicomponent alloy. 07 2022. doi:[10.13140/RG.2.2.14298.00967](https://doi.org/10.13140/RG.2.2.14298.00967).
- Hendrik J. Monkhorst and James D. Pack. Special points for brillouin-zone integrations. *Phys. Rev. B*, 13:5188–5192, 1976.
- Ryoichi Monzen, Takasumi Hosoda, Yusaku Takagawa, and Chihiro Watanabe. Bend formability and strength of cu–be–co alloys. *Journal of Materials Science*, 46(12):4284–4289, 2011.
- Bohayra Mortazavi, Evgeny Podryabinkin, Ivan S Novikov, Stephan Roche, Timon Rabczuk, Xiaoying Zhuang, and Alexander Shapeev. Efficient machine-learning based interatomic potentials for exploring thermal conductivity in two-dimensional materials. *Journal of Physics: Materials*, 2020a.
- Bohayra Mortazavi, Evgeny V Podryabinkin, Stephan Roche, Timon Rabczuk, Xiaoying Zhuang, and Alexander V Shapeev. Machine-learning interatomic potentials enable first-principles multiscale modeling of lattice thermal conductivity in graphene/borophene heterostructures. *Materials Horizons*, 7(9):2359–2367, 2020b.
- Bohayra Mortazavi, Evgeny V Podryabinkin, Ivan S Novikov, Timon Rabczuk, Xiaoying Zhuang, and Alexander V Shapeev. Accelerating first-principles estimation of thermal conductivity by machine-learning interatomic potentials: A mtp/shengbte solution. *Computer Physics Communications*, 258:107583, 2021.
- Anastasia S Naumova, Sergey V Lepeshkin, Pavel V Bushlanov, and Artem R Oganov. Unusual chemistry of the c–h–n–o system under pressure and implications for giant planets. *The Journal of Physical Chemistry A*, 125(18):3936–3942, 2021.
- Lance J. Nelson, Vidvuds Ozoliņš, C. Shane Reese, Fei Zhou, and Gus L. W. Hart. Cluster expansion made easy with bayesian compressive sensing. *Phys. Rev. B*, 88:155105, 2013.
- C Niu, AJ Zaddach, AA Oni, X Sang, JW Hurt, JM LeBeau, CC Koch, and DL Irving. Spin-driven ordering of cr in the equiatomic high entropy alloy nifecro. *Applied Physics Letters*, 106(16), 2015.
- J. Nocedal and S. Wright. *Numerical Optimization*. Springer, 2006.
- Ivan Novikov, Blazej Grabowski, Fritz Kormann, and Alexander Shapeev. Magnetic moment tensor potentials for collinear spin-polarized materials reproduce different magnetic states of bcc fe, 2021.
- T. Omori, J. Sato, K. Shinagawa, I. Ohnuma, K. Oikawa, R. Kainuma, and K. Ishida. Experimental determination of phase equilibria in the co-cr-ni system. *Journal of Phase Equilibria and Diffusion*, 35(2):178–185, 2014.

- Ivan Oseledets. Tensor-train decomposition. *SIAM J. Scientific Computing*, 33: 2295–2317, 01 2011.
- Corey Oses, Cormac Toher, and Stefano Curtarolo. High-entropy ceramics. *Nature Reviews Materials*, 5(4):295–309, 2020.
- L.R. Owen, E.J. Pickering, H.Y. Playford, H.J. Stone, M.G. Tucker, and N.G. Jones. An assessment of the lattice strain in the crmnfeconi high-entropy alloy. *Acta Materialia*, 122:11–18, 2017.
- Alexander Ya. Pak, Vadim Sotskov, Arina A. Gumovskaya, Yuliya Z. Vassilyeva, Zhanar S. Bolatova, Yulia A. Kvashnina, Gennady Ya. Mamontov, Alexander V. Shapeev, and Alexander G. Kvashnin. Machine learning-driven synthesis of TiZrNbHfTaC₅ high-entropy carbide. *npj Computational Materials*, 9(1):7, 2023.
- Zongrui Pei, Rui Li, Michael C. Gao, and G. Malcolm Stocks. Statistics of the nicocr medium-entropy alloy: Novel aspects of an old puzzle. *npj Computational Materials*, 6(1):122, 2020.
- John P. Perdew, J. A. Chevary, S. H. Vosko, Kobljar A. Jackson, Mark R. Pederson, D. J. Singh, and Carlos Fiolhais. Atoms, molecules, solids, and surfaces: Applications of the generalized gradient approximation for exchange and correlation. *Phys. Rev. B*, 46:6671–6687, 1992.
- John P. Perdew, Kieron Burke, and Matthias Ernzerhof. Generalized gradient approximation made simple. *Phys. Rev. Lett.*, 77:3865–3868, 1996.
- Ed Pickering and Nicholas Jones. High-entropy alloys: A critical assessment of their founding principles and future prospects. *International Materials Reviews*, 61, 05 2016.
- Evgeny V Podryabinkin, Evgeny V Tikhonov, Alexander V Shapeev, and Artem R Oganov. Accelerating crystal structure prediction by machine-learning interatomic potentials with active learning. *Physical Review B*, 99(6):064114, 2019.
- W. Press, S. Teukolsky, W. Vetterling, and B. Flannery. *Numerical Recipes in C*. Cambridge University Press, 1992.
- Roberto J. Rioja and John Liu. The evolution of al-li base products for aerospace and space applications. *Metallurgical and Materials Transactions A*, 43(9):3325–3337, 2012.
- Christian Robert and George Casella. *Metropolis–Hastings Algorithms*, pages 167–197. 01 1970. ISBN 978-1-4419-1582-5.
- Michaela Roudnicka, Jiri Bigas, Orsolya Molnarova, David Palousek, and Dalibor Vojtech. Different response of cast and 3d-printed co-cr-mo alloy to heat treatment: A thorough microstructure characterization. *Metals*, 11(5), 2021.

- L. Rudolf Kanyane, A. Patricia Popoola, and Nicholus Malatji. Development of spark plasma sintered tialsimow multicomponent alloy: Microstructural evolution, corrosion and oxidation resistance. *Results in Physics*, 12:1754–1761, 2019.
- J. M. Sanchez. Cluster expansion and the configurational theory of alloys. *Phys. Rev. B*, 81:224202, 2010.
- Tamar Schlick. *Molecular Modeling and Simulation: An Interdisciplinary Guide, Interdisciplinary Applied Mathematics Vol. 21*. Springer-Verlag, 2002.
- Dmitrii V. Semenov, Alexander G. Kvashnin, Ivan A. Kruglov, and Artem R. Oganov. Actinium hydrides ach10, ach12, and ach16 as high-temperature conventional superconductors. *The Journal of Physical Chemistry Letters*, 9(8):1920–1926, 2018.
- L. J. Sham and W. Kohn. One-particle properties of an inhomogeneous interacting electron gas. *Phys. Rev.*, 145:561–567, 1966.
- A. Shapeev. Accurate representation of formation energies of crystalline alloys with many components. *Computational Materials Science*, 139:26–30, 2017.
- Alexander V. Shapeev. Moment tensor potentials: A class of systematically improvable interatomic potentials. *Multiscale Modeling & Simulation*, 14(3):1153–1173, 2016.
- Seok Su Sohn, Dong Geun Kim, Yong Hee Jo, Alisson Kwiatkowski da Silva, Wenjun Lu, Andrew John Breen, Baptiste Gault, and Dirk Ponge. High-rate superplasticity in an equiatomic medium-entropy vconi alloy enabled through dynamic recrystallization of a duplex microstructure of ordered phases. *Acta Materialia*, 194:106–117, 2020.
- Vadim Sotskov, Evgeny V. Podryabinkin, and Alexander V. Shapeev. A machine-learning potential-based generative algorithm for on-lattice crystal structure prediction. *Journal of Materials Research*, 2023.
- Tomasz Stasiak, Mourtada Aly Sow, Matthieu Touzin, Franck Béclin, and Catherine Cordier. Powder metallurgy processing and characterization of the δ phase containing multicomponent al-cr-fe-mn-mo alloy. *Alloys*, 2(1):44–54, 2023.
- Larisa Stepanova and S Bronnikov. Molecular dynamics modeling of crack propagation. *Journal of Physics: Conference Series*, 1368:042039, 11 2019.
- Daniel Svensson. High entropy alloys: Breakthrough materials for aero engine applications? 2015.
- Artur Tamm, Alvo Aabloo, Mattias Klintonberg, Malcolm Stocks, and Alfredo Caro. Atomic-scale properties of ni-based fcc ternary, and quaternary alloys. *Acta Materialia*, 99:307–312, 2015.
- L. E. Tanner, H. Okamoto, and T. Nishizawa. The be-co (beryllium-cobalt) system. *Bulletin of Alloy Phase Diagrams*, 9(5):552–562, 1988.

- Atsushi Togo, Fumiyasu Oba, and Isao Tanaka. First-principles calculations of the ferroelastic transition between rutile-type and CaCl_2 -type SiO_2 at high pressures. *Phys. Rev. B*, 78:134106, 2008.
- Y. Tong, G. Velisa, T. Yang, K. Jin, C. Lu, H. Bei, J. Y. P. Ko, D. C. Pagan, R. Huang, Y. Zhang, L. Wang, and F. X. Zhang. Probing local lattice distortion in medium- and high-entropy alloys, 2017.
- K.-Y. Tsai, M.-H. Tsai, and J.-W. Yeh. Sluggish diffusion in co-cr-fe-mn-ni high-entropy alloys. *Acta Materialia*, 61(13):4887–4897, 2013.
- J. G. Valatin. Generalized hartree-fock method. *Phys. Rev.*, 122:1012–1020, 1961.
- Flynn Walsh, Mark Asta, and Robert O. Ritchie. Magnetically driven short-range order can explain anomalous measurements in crconi, 2021.
- Michael Widom. *Prediction of Structure and Phase Transformations*, pages 267–298. 2016.
- Michael Widom. Modeling the structure and thermodynamics of high-entropy alloys. *Journal of Materials Research*, 33(19):2881–2898, 2018.
- Jonathan T. Willman, Ashley S. Williams, Kien Nguyen-Cong, Aidan P. Thompson, Mitchell A. Wood, Anatoly B. Belonoshko, and Ivan I. Oleynik. Quantum accurate SNAP carbon potential for MD shock simulations. *AIP Conference Proceedings*, 2272(1), 2020.
- Henry Wu, Tam Mayeshiba, and Dane Morgan. High-throughput ab-initio dilute solute diffusion database. *Scientific Data*, 3(1):160054, 2016.
- Xiao Yang and Yong Zhang. Prediction of high-entropy stabilized solid-solution in multi-component alloys. *Materials Chemistry and Physics*, 132:233–238, 02 2012.
- Xi Yao, Congwei Xie, Xiao Dong, Artem R. Oganov, and Qingfeng Zeng. Novel high-pressure calcium carbonates. *Phys. Rev. B*, 98:014108, 2018.
- J-W Yeh, S-K Chen, S-J Lin, J-Y Gan, T-S Chin, T-T Shun, C-H Tsau, and S-Y Chang. Nanostructured high-entropy alloys with multiple principal elements: novel alloy design concepts and outcomes. *Advanced engineering materials*, 6(5): 299–303, 2004.
- Binglun Yin, Shuhei Yoshida, Nobuhiro Tsuji, and W Curtin. Yield strength and misfit volumes of nicocr and implications for short-range-order. *Nature Communications*, 11:2507, 05 2020.
- Xiao-Xiang Yu, Gregory B Thompson, and Christopher R Weinberger. Influence of carbon vacancy formation on the elastic constants and hardening mechanisms in transition metal carbides. *Journal of the European Ceramic Society*, 35(1):95–103, 2015.

- Ruopeng Zhang, Shiteng Zhao, Jun Ding, Yan Chong, Tao Jia, Colin Ophus, Mark Asta, Robert O. Ritchie, and Andrew M. Minor. Short-range order and its impact on the crconi medium-entropy alloy. *Nature*, 581(7808):283–287, 2020.
- Weiwei Zhang, Artem R. Oganov, Qiang Zhu, Sergey S. Lobanov, Elissaios Stavrou, and Alexander F. Goncharov. Stability of numerous novel potassium chlorides at high pressure. *Scientific Reports*, 6(1):26265, 2016.
- Xinghang Zhang, Khalid Hattar, Youxing Chen, Lin Shao, Jin Li, Cheng Sun, Kaiyuan Yu, Nan Li, Mitra L Taheri, Haiyan Wang, et al. Radiation damage in nanostructured materials. *Progress in Materials Science*, 96:217–321, 2018.
- Yanhui Zhang, Yu Zhuang, Alice Hu, J.J. Kai, and C.T. Liu. The origin of negative stacking fault energies and nano-twin formation in face-centered cubic high entropy alloys. *Scripta Materialia*, 130:96–99, 03 2017.
- Yang Zhou, Philip Nash, Samuel M. Bessa, Guilherme Teodoro Ferrigatto, Bruna Santos V. P. Madureira, Aparecida Silva Magalhães, Aline Oliveira, Guilherme Carvalho Pereira, Lorena Goncalves Ribeiro, Lucas Pires dos Santos, André Alves da Silva, Jessica Dornelas Silva, Andre Gonzalez Silva, Jean Muniz de Souza, Yuri Santorio Torres, Raul Lima da Silva, and Barbara Fernanda Rievers Fernandes de Cunha. Phase equilibria in the al-co-ni alloy system. *Journal of Phase Equilibria and Diffusion*, 38(5):630–645, 2017.